Weakening of the Gulf Stream at Florida Straits over the past century inferred from coastal sea-level data

Christopher Piecuch[1]

[1]Woods Hole Oceanographic Institution

November 30, 2022

Abstract

The Florida Current marks the beginning of the Gulf Stream at Florida Straits, and plays an important role in climate. Nearly continuous measurements of Florida Current transport have been made at ~27N since 1982, but these data are too short to allow an assessment of possible centennial changes. Here I reconstruct Florida Current transport during 1909-2018 using probabilistic methods and principles of ocean dynamics applied to available transport measurements and longer coastal sea-level data. The Florida Current transport very likely (probability P=0.93) has weakened since the 1920s, such that modern measurements made within Florida Straits since 1982 likely (P=0.87) portray the transport in a reduced state. The weakest decadally averaged transport during the last 110 y probably (P=0.74) took place sometime in the last two decades. Weakening of Florida Current transport is consistent with a hypothesized steady reduction of the deep Atlantic meridional overturning circulation during the past century.

Coversheet for "Weakening of the Gulf Stream at Florida Straits over the past century inferred from coastal sea-level data"

Christopher G. Piecuch[1,†]

[1]*Department of Physical Oceanography, Woods Hole Oceanographic Institution, Woods Hole, Massachusetts, USA*

This paper is a non-peer reviewed preprint submitted to Earth and Space Science Open Archive (ESSOAr). The paper is under review at Nature Communications.

† cpiecuch@whoi.edu

Weakening of the Gulf Stream at Florida Straits over the past century inferred from coastal sea-level data

Christopher G. Piecuch[1]

[1] *Woods Hole Oceanographic Institution, Woods Hole, Massachusetts, USA*

The Florida Current marks the beginning of the Gulf Stream at Florida Straits, and plays an important role in climate. Nearly continuous measurements of Florida Current transport have been made at $\sim 27°$N since 1982, but these data are too short to allow an assessment of possible centennial changes. Here I reconstruct Florida Current transport during 1909–2018 using probabilistic methods and principles of ocean dynamics applied to available transport measurements and longer coastal sea-level data. The Florida Current transport very likely (probability $P = 0.93$) has weakened since the 1920s, such that modern measurements made within Florida Straits since 1982 likely ($P = 0.87$) portray the transport in a reduced state. The weakest decadally averaged transport during the last 110 y probably ($P = 0.74$) took place sometime in the last two decades. Weakening of Florida Current transport is consistent with a hypothesized steady reduction of the deep Atlantic meridional overturning circulation during the past century.

Swiftly flowing north through the narrow, shallow Florida Straits, the Florida Current marks the headwaters of the Gulf Stream[1–4] (Figure 1). Together with the weaker Antilles Current[5], the Florida Current forms the major western boundary current in the subtropical North Atlantic Ocean at 27°N, providing closure to the wind-driven interior gyre circulation[6,7], and acting as a vital limb of the Atlantic meridional overturning circulation[8]. Due to its transport of heat and other tracers, the Florida Current plays an important role in climate[9,10].

The integrated volume transport of the Florida Current (hereafter Florida Current transport) has been monitored nearly continuously at $\sim 27°$N since 1982 by means of abandoned submarine telephone cables between West Palm Beach and Grand Bahama Island[1–4] (Figure 1). Before then, observations were made occasionally as part of short hydrographic cruises or brief field campaigns, each measuring a different component of the flow at a different location. Earlier observations[11,12] only measured the near-surface transports, but missed transports at depth. Later full-depth transport measurements[13–16] were made variously between Florida and Havana, Cay Sal Bank, the Cat Cays, or Bimini, capturing flow through Yucatán Channel, but omitting flows through Nicholas, Santaren, or Northwest Providence Channels, all of which contribute to the transport at 27°N (Figure 1). Such disparities make it difficult to produce a stable instrumental estimate of Florida Current transport through time. Without such a coherent, longterm estimate, it has been unclear whether the Florida Current has undergone multidecadal- or longer-timescale change. Meinen et al.[2] concluded that the extant data, "provide no evidence for a longterm trend in the Florida Current transport," during 1964–2009. However, it remains unclear whether a trend would emerge in a longer, more complete transport history.

Questions of possible longterm changes in Florida Current transport bear on hypotheses that the Atlantic meridional overturning circulation is weakening or has weakened. Proxy indicators, including surface and subsurface ocean temperatures at subpolar latitudes and sortable silts from sediment cores off Cape Hatteras, suggest that the deep return flow of the meridional overturning circulation weakened either continuously during the twentieth century or earlier at the end of the Little Ice Age[17–19]. Yet, uncertainties in the proxies and their relationship to overturning render the robustness of these suggestions unclear. Models simulate that, under climate change, a slowing of the deep overturning circulation is balanced by a weakening surface western boundary current[20,21]. A determination of whether the Florida Current transport changed over the past century would thus serve as a test of both model simulations and hypotheses of a reduced deep overturning.

Previous authors reasoned that sea level from coastal tide gauges is informative of changes in Florida Current transport[12,14,22,23]. These arguments are predicated on the notion of geostrophic balance—on timescales longer than a day, the northward flow through Florida Straits imparts an eastward acceleration owing to the Coriolis force that is counteracted by a pressure gradient across the Florida Straits, which manifests as a sea-level difference that can be observed by tide gauges on opposite sides of the Florida Current. However, circulation inferences based on tide gauges need to be made cautiously. Tide gauges measure the distance between the sea surface and Earth's crust at the coast. So, they observe not only large-scale ocean dynamics, but also coastally trapped signals[24] and isostatic geophysical phenomena, including changes in the planet's gravity field and rotation vector, and viscoelastic deformation of the solid Earth[25]. Tide-gauge data are also heterogeneously distributed in space and time. Long, continuous records are available at some southeastern USA and Caribbean sites far afield of the submarine cable at 27°N, but extant records from tide gauges close to the cable's endpoints near West Palm Beach and Grand Bahama are short, incomplete, and largely not overlapping with one another[26].

To overcome these challenges, I use probabilistic data assimilation[27,28] to estimate annual Florida Current transport at 27°N over the past 110 y (see Methods). The estimate is based on 1,390 y of annual coastal sea level from 46 tide gauges[26] in the southeastern USA and Caribbean during 1909–2018 (Figure 1a) and 37 y of annual Florida Current transport from cable measurements[1–4] since 1982 (Figure 2a). Sea level is represented as a process with spatial correlation and temporal memory. The Florida Current transport is related to the difference in sea level across Florida Straits through geostrophy, but account is also taken of non-oceanographic and ageostrophic impacts on sea level and transport. The data are cast as corrupt, imperfect versions of the processes. Bayes' rule is used to invert the model equations, and solutions are generated using numerical methods. The model equations are coupled, sharing information across space, time, and processes, allowing data gaps to be filled and unobserved processes to be estimated. The solution is fully probabilistic, and comprises thousands of ensemble members, each an equally likely history of transport that is consistent with the data and model equations. This allows the calculation of subtle spatiotemporal statistics, for example, the probability density function of the magnitude or timing of the minimum or maximum decadally averaged transport value during the study period (see Methods). Residual analyses and synthetic data experiments demonstrate the appropriateness of the algorithm and show that it accurately estimates the quantities of interest given the data (cf. Supplementary Information).

Weakening of the Florida Current

The probabilistic Florida Current transport reconstruction is summarized in Figure 2a. The 110-y mean transport is 32.6 ± 1.4 Sv (Supplementary Figure 1a), which is likely (probability $P = 0.87$)

larger than the mean over 1982–2018 (31.8 ± 0.1 Sv). This implies that the cable data[1–4] probably represent the Florida Current in a reduced state of transport. Unless otherwise stated, $\pm$ values are 95% posterior credible intervals estimated from the Bayesian model. Estimated uncertainties since 1982 are comparatively small, and essentially reflect instrumental errors on the cable data, which place strong observational constraints on the process. Before then, cable data are unavailable, and the inference is largely constrained by tide gauge data, which have a more uncertain relationship to the transport and are sparser earlier in time, resulting in larger errors that grow into the past.

Superimposed on the mean are interannual-to-decadal fluctuations in transport (Figure 2a). The standard deviation of annual transports is 1.3 Sv (posterior median estimate). A 3.3 ± 1.1 Sv weakening from 1997–1998 to 1999–2000, when there was a gap in cable measurements and low transports were seen upstream in Yucatán Channel[29], was followed by a 2.5 ± 1.1 Sv strengthening from 1999–2000 to 2001–2002 (Supplementary Figure 1c). Decadal-average transport was likely ($P \geq 0.79$) greater than the longterm average during 1922–1932 (33.6 ± 2.8 Sv) and 1956–1966 (33.0 ± 1.7 Sv), but less than average in 1946–1956 (32.2 ± 2.0 Sv) and 1986–1996 (31.7 ± 0.2 Sv) (Supplementary Figure 1d). A wavelet coherence analysis demonstrates that transport fluctuations can be related to major modes of surface climate variation (Supplementary Figure 2). The transport is probably ($P > 68\%$) coherent with the North Atlantic Oscillation[30] at 2–8-y periods centered between the late 1970s and early 2000s, consistent with past studies of cable data[1,31]; coherence is also found at 2–4-y periods around 1960 and 8-y periods between the late 1930s and early 1950s, which have not been previously reported, and possibly result from changes in subtropical wind curl mediated by planetary waves[31]. Transport is also likely ($P > 0.68$) coherent with Atlantic

Multidecadal Variability[32] at 2–16-y periods centered on the mid 1990s and 16-y periods from the late 1940s to early 2000s. The weaker coherence earlier in time could reflect nonstationarity in the relationship between transport and climate, or the growth in transport uncertainties into the past.

Changes are also apparent on the longest timescales. The transport trend during 1909–2018 is -1.7 ± 3.7 Sv century^{-1}, which overlaps zero, but implies that transport likely ($P = 0.82$) declined (Supplementary Figure 1b). This inference of a longterm weakening is qualitatively insensitive to the selection of time period. Computing differences between all pairs of decadal averages, I find most (67%) instances are such that transport probably ($P > 0.68$) declined from one decade to another (Figure 3). For example, it is very likely ($P = 0.93$) transport weakened from 1920–1930 (2.1 ± 2.9 Sv), and extremely likely ($P = 0.96$) that it declined from 1970–1980 (1.2 ± 1.2 Sv) to the present more than expected from a stationary red-noise process. Indeed, if the transport was stationary, extrema would be uniformly likely to occur at any point over a given time period, while in the presence of a longterm decline, the maximum transport would be more likely to occur at the beginning and the minimum transport at the end of the period. Consistent with the latter case, the minimum decadal-average transport (31.1 ± 1.0 Sv) likely ($P = 0.74$) started sometime after 2002, and the maximum decadal average (34.1 ± 2.5 Sv) likely ($P = 0.70$) ended some year before 1936 (Figure 2b). Timing of the extrema cannot be explained in terms of fluctuations about a stationary mean. After subtracting the longterm trend (Supplementary Figure 1b), I find that it would have been unlikely ($P = 0.18$) that the minimum transport would have started after 2002, and chances would have been lower ($P = 0.38$) that the maximum would have ended before 1936 (Figure 2c).

Relation Between Florida Current Transport and Sea-Level Difference Across Florida Straits

In addition to transport (Figure 2a), the Bayesian algorithm also solves for the regression coefficient between the transport and sea-level difference across Florida Straits (see Methods). The estimated change in transport per unit change in sea-level difference is 0.21 ± 0.11 Sv cm^{-1} (Supplementary Figure 3a). Geostrophy allows interpretation of this value in terms of an effective depth describing the vertical scale over which velocity variations decay in amplitude from the surface to the bottom within Florida Straits[33,34]. Following Little et al.[34], I multiply by the ratio of the Coriolis parameter over gravity ($\sim 7{\times}10^{-6}$ s m^{-1} at 27°N), obtaining an effective depth of $144{\pm}74$ m. This estimate is consistent with the vertical structure of northward currents observed *via* shipboard acoustic doppler current profiler aboard the R/V Walton Smith during 70 cruises across Florida Straits at 27°N over 2001–2018. At the longitude of the core of the current, the average meridional velocity taken over all cruises decays almost linearly in the vertical from ~ 1.2 m s^{-1} near the surface to ~ 0.9 m s^{-1} and ~ 0.6 m s^{-1} at 200- and 400-m depth, respectively (Figure 4a). Computing standard deviations in meridional velocity over cruises, I find that flow-variation amplitudes decay more exponentially with depth, decreasing rapidly from ~ 0.6 m s^{-1} near the surface to ~ 0.3 m s^{-1} and ~ 0.2 m s^{-1} at 200- and 400-m depth, respectively (Figure 4b). Similar vertical structures of mean and variable meridional currents were reported based on earlier observations made during 1982–1984 as part of the Subtropical Atlantic Climate Studies Program[35].

I have assumed that the regression coefficient between sea level and transport is time invariant (see Methods). To test whether this assumption is reasonable, I compute coherence and admittance between sea level and transport output from an ocean reanalysis product[36] spanning 1871–2010. Considering interannual to multidecadal periods, I find that transports and sea-level differences are coherent across all accessible timescales, such that the admittance amplitude (transfer function) is qualitatively insensitive to frequency band, and that the change in transport per a unit change in the sea-level difference is similar for interannual and multidecadal periods (Supplementary Figure 4). Importantly, I also find that the Bayesian algorithm successfully estimates the correct regression coefficient between the two quantities in a synthetic data experiment based on this ocean reanalysis product (see Supplementary Information). These findings suggest that assuming a constant-in-time relationship between transport and sea-level difference is reasonable, and that my model correctly estimates the relationship between the two quantities given the available data.

Distinguishing Dynamic and Static Sea-Level Differences Across Florida Straits

The meaningfulness of the transport estimate hinges on the model's ability to identify and separate dynamic and static components of the sea-level difference across the Florida Straits. The posterior solution for the 110-y trend in sea-level difference across the Florida Straits (Grand Bahama minus West Palm Beach) is -0.2 ± 1.0 mm y^{-1} (Supplementary Figure 3b). This trend results from the competing influences of a dynamic trend in sea-level difference of -0.9 ± 2.2 mm y^{-1} and a static trend of 0.7 ± 2.3 mm y^{-1} (Supplementary Figure 3b), which I interpret respectively as indicating differential trends in sea-surface height and vertical land motion across Florida Straits.

Several lines of independent observational evidence corroborate these model inferences based on data from tide gauges and submarine cables. The Global Positioning System (GPS) provides an instrumental means for measuring vertical land motion. Version 6a of the dataset from Université de la Rochelle[37] provides continuous GPS records from three locations in southeastern Florida and two Bahamas locations (Supplementary Figure 5; Supplementary Table 1). Computing the average vertical velocity for the two Bahamas sites, and doing the same over the three sites in southeastern Florida, I determine after taking the difference that sea level is statically rising 1.0 ± 1.3 mm y^{-1} faster in the Bahamas than along southeastern Florida owing to differential land subsidence, where the $\pm$ value is twice the estimated standard error, assuming that the standard errors provided with the data are independent (Supplementary Table 1). This rate is consistent with the static trend in the sea-level difference across Florida Straits determined by the Bayesian model.

Proxy records of sea level are informative of background rates of change unrelated to ocean dynamics. I consider recent standardized compilations of Holocene sea-level index points from the Caribbean and southeastern USA derived from coral reefs, mangrove peats, and other indicators[38,39]. To estimate present-day rates of background change unrelated to circulation and climate, I consider only the locations in the databases that have at least three sea-level index points with best-estimate ages between 2,000 and 150 y before present. This criterion is satisfied by two sites in southeastern Florida and one site in the Bahamas (Supplementary Figure 5; Supplementary Table 2). Taking the difference between the linear trend fit to the index points from the Bahamas site and the average of the trends fit to the data at the two southeastern Florida locations, I estimate that sea level rose 0.6 ± 0.6 mm y^{-1} more rapidly in the Bahamas relative to southeastern Florida in the pre-industrial Common Era (Supplementary Table 2), where the $\pm$ value is twice the standard error furnished by ordinary least squares applied to the best estimates of proxy age and sea level. Interpreted in terms of differential land motion, this sea-level trend difference revealed by proxy data suggests that the difference in rates of vertical land motion between the Bahamas and southeastern Florida observed by GPS is, at least partly, due to background geological effects (e.g., glacial isostatic adjustment).

Modern radar altimeters have observed sea-surface height over nearly the global ocean since 1993. Once adjusted for static effects, altimeter data can be interpreted in terms of surface currents. I consider time series of along-track sea-surface height processed by the Centre of Topography of the Oceans and the Hydrosphere[40] at the altimeter data points closest to Settlement Point on Grand Bahama Island and Virginia Key in southeastern Florida (Supplementary Figure 5). Differencing the two altimetric time series and fitting a linear trend, I determine that the average rate of change in the sea-surface-height difference across Florida Straits over 1993–2017 was -2.2 ± 3.0 mm y^{-1} (Supplementary Figure 6), where the $\pm$ value is twice the standard error estimated accounting for residual autocorrelation using repeated simulations with surrogate data[41]. This rate from altimetry, while reflecting a relatively short period, basically agrees in sign and magnitude with the dynamic trend in sea-level difference across Florida Straits inferred by the Bayesian model. Note that, while it is closer to the western end of the submarine cable than Virginia Key, the West Palm Beach gauge is not considered in this exercise based on altimetry data; given the geometry of the satellite tracks, the closest altimeter data point to the latter gauge is ~ 50 km offshore, east of the Florida Current core (cf. Figure 4; Supplementary Figure 5), and does not reflect sea level at the western boundary.

Relation to Wind Stress and the Interior Gyre

Assuming no changes in Bering Straits throughflow or evaporation and precipitation over the basin, weakening of the Florida Current transport must have been balanced by changes in the interior gyre or overturning transports at 27°N. To explore possible changes in the gyre, I calculate geostrophic Sverdrup streamfunction[6] using wind-stress curl from two reanalyses of the twentieth century[42,43]. Both yield a climatological southward transport of ~ -23 Sv at 27°N over 1900–2010 (Figure 5a), consistent with basic expectations[44]. However, the two reanalyses give conflicting trend estimates, with one[42] yielding a weaker northward trend of 1.9 ± 2.0 Sv century^{-1}, and the other[43] a stronger southward trend of -4.2 ± 1.3 Sv century^{-1} across 27°N (Figure 5b) where the $\pm$ values are formal estimates of the 95% confidence interval adjusted for residual autocorrelations[41]. Discrepancies are apparent broadly over the subtropics, with one reanalysis product[43] suggesting spin-up of the gyre, and the other[42] spin-down. These results are unaffected if ageostrophic Ekman transports are also included in the calculation (Figure 5b).

Relation to the Deep Overturning

The longterm weakening of the Florida Current found here is comparable to the slowing of the deep overturning circulation hypothesized to have occurred over the past century[17–19]. These hypotheses are partly based on the facts that models consistently show strong correlation between overturning streamfunction and sea-surface temperature in the North Atlantic subpolar gyre on decadal and longer timescales[17,18,45,46], and that observations show a "warming hole" over the subpolar gyre, where sea-surface temperatures have recently fallen by 0.3–0.9°C century^{-1} relative to the global average[43,47,48] (Figure 6).

To test whether the inferred weakening of the Florida Current, observed surface cooling over the subpolar gyre, and hypothesized slowdown of the deep overturning are all physically consistent with one another, I consider a simple ocean heat budget for the North Atlantic poleward of 27°N (see Supplementary Information). I assume that decreasing ocean heat transport across 27°N due to the combined weakening of the Florida Current and deep overturning is largely balanced by increasing surface turbulent (sensible and latent) heat gain across the northern North Atlantic due to the cooling sea-surface temperatures[49]. Ignoring local heat storage, the sea-surface-temperature change per unit change in transport is a function of the background mean sea-surface temperature, vertical temperature stratification, and surface wind speed over the study region, along with the area across which surface cooling takes place (see Supplementary Information). Choosing reasonable parameter ranges, I derive a rough, first-principles estimate of 0.3–0.6°C Sv^{-1}. This is similar to values of 0.2–0.5°C Sv^{-1} found independently by dividing the observed sea-surface-temperature trends across the subpolar gyre (Figure 6) by the posterior median estimate of the trend in Florida Current transport over the past century (Supplementary Figure 1b). These numbers agree with a range of 0.2–0.6°C Sv^{-1} published based on regression analyses of sea-surface temperature and overturning streamfunction from climate models[17,18,45,46].

Conclusions

Lack of knowledge about decadal and longer trends in ocean currents has been a key observational uncertainty related to climate change. I used Bayesian data analysis[27,28] to assimilate data from submarine cables and tide gauges and to infer the evolution of the Florida Current transport at 27°N during 1909–2018. I found that Florida Current transport probably declined over the last 110 y, such that modern submarine cable data likely represent transport in a relatively reduced state, and that the weakest decadal transport since the turn of the twentieth century probably occurred in the last two decades. Results are consistent with observed cooling across the subpolar sea surface and suggestions of a continuous decline in the deep overturning circulation over the past century, and lend support to model predictions that a reduction of the deep overturning cell under climate change is mirrored by a slowdown of the surface western boundary current.

Future studies should identify what caused the weakening of Florida Current transport, and constrain whether changes in upper mid-ocean transports also took place. While systematic issues with current reanalyses preclude conclusive results, possible longterm changes in the wind-driven gyre circulation cannot be ruled out. Likewise, a recent data analysis[5] determined that the Antilles Current is highly variable on interannual and shorter timescales over 2005–2015, but that current's behavior across decadal and longer timescales is unclear. Future efforts should also build upon this Bayesian modeling framework to incorporate altimetric observations, GPS data, and proxy records to better constrain the inference and reduce uncertainty.

1. Baringer, M. O., and J. C. Larsen. Sixteen Years of Florida Current Transport at 27°N, *Geophys. Res. Lett.*, **28**, 317–3182 (2001).

2. Meinen, C. S., M. O. Baringer, and R. F. Garcia. Florida Current transport variability: An analysis of annual and longer-period signals, *Deep-Sea Res.*, **57**, 835–846 (2010).

3. Larsen, J. C. Transport and heat flux of the Florida Current at 27°N derived from cross-stream voltages and profiling data: theory and observations, *Phil. Trans. R. Soc. A.*, **338**, 169–236 (1992).

4. Garcia, R. F., and C. S. Meinen. Accuracy of Florida Current Volume Transport Measurements at 27°N Using Multiple Observational Techniques, *J. Atmos. Ocean. Tech.*, **31**, 1169–1180 (2014).

5. Meinen, C. S., et al. Structure and Variability of the Antilles Current at 26.5°N, *J. Geophys. Res.-Oceans*, **124**, 3700–3723 (2019).

6. Sverdrup, H. U. Wind-Driven Currents in a Baroclinic Ocean; With Application to the Equatorial Currents of the Eastern Pacific, *Proc. Natl. Acad. Sci. U.S.A.*, **33**, 318–326 (1947).

7. Stommel, H. The Westward Intensification of Wind-Driven Ocean Currents, *EOS T. Am. Geophys. Un.*, **29**, 202–206 (1948).

8. McCarthy, G. D., et al. Measuring the Atlantic Meridional Overturning Circulation at 26°N, *Prog. Oceanogr.*, **130**, 91–111 (2015).

9. Lynch-Stieglitz, J. The Atlantic Meridional Overturning Circulation and Abrupt Climate Change, *Annu. Rev. Mar. Sci.*, **9**, 83–104 (2017).

10. Palter, J. B. The Role of the Gulf Stream in European Climate, *Annu. Rev. Mar. Sci.*, **7**, 113–137 (2015).

11. Pillsbury, J. E. The Gulf Stream—a description of the methods employed in the investigation, and the results of the research, *Rept. Supt., US Coast Geod. Surv.*, **Appendix 10**, 461–620 (1890).

12. Hela, I. The Fluctuations of the Florida Current, *B. Mar. Sci. Gulf Carib.*, **1**, 241–248 (1952).

13. Schmitz, W. J., and W. S. Richardson. On the transport of the Florida Current, *Deep-Sea Res.*, **15**, 679–693 (1968).

14. Wunsch, C., D. V. Hansen, and B. D. Zetler. Fluctuations of the Florida Current inferred from sea level records, *Deep-Sea Res.*, **16**, 447–470 (1969).

15. Niiler, P. P., and W. S. Richardson. Seasonal Variability of the Florida Current, *J. Mar. Res.*, **31**, 144–167 (1973).

16. Brooks, I. H., and P. P. Niiler. Energetics of the Florida Current, *J. Mar. Res.*, **35**, 163–191 (1977).

17. Rahmstorf, S., et al. Exceptional twentieth-century slowdown in Atlantic Ocean overturning circulation, *Nature Clim. Change*, **5**, 475–480 (2015).

18. Caesar, L., S. Rahmstorf, A. Robinson, G. Feulner, and V. Saba. Observed fingerprint of a weakening Atlantic Ocean overturning circulation, *Nature*, **556**, 191–196 (2018).

19. Thornalley, D. J. R., et al. Anomalously weak Labrador Sea convection and Atlantic overturning during the past 150 years, *Nature*, **556**, 227–230 (2018).

20. Thomas, M. D., et al. Upper ocean manifestations of a reducing meridional overturning circulation, *Geophys. Res. Lett.*, **39**, L16609 (2012).

21. Beadling, R. L., et al. Evaluation of Subtropical North Atlantic Ocean Circulation in CMIP5 Models against the Observational Array at $26.5°$N and Its Changes under Continued Warming, *J. Clim.*, **31**, 9697–9718 (2018).

22. Maul, G. A., et al. Sea Level Variation as an Indicator of Florida Current Volume Transport: Comparisons with Direct Measurements, *Science*, **227**, 304–307 (1985).

23. Park, J., and W. Sweet. Accelerated sea level rise and Florida Current transport, *Ocean Sci.*, **11**, 607–615 (2015).

24. Brink, K. H. Coastal-Trapped Waves and Wind-Driven Currents over the Continental Shelf, *Annu. Rev. Fluid Mech.*, **23**, 389–412.

25. Tamisiea, M. E., and J. X. Mitrovica. The moving boundaries of sea level change: Understanding the origins of geographic variability, *Oceanography*, **24**, 24–39 (2011).

26. Holgate, S. J., et al. New Data Systems and Products at the Permanent Service for Mean Sea Level, *J. Coastal Res.*, **29**, 3, 493–504 (2013).

27. Tingley, M. P., et al. Piecing together the past: statistical insights into paleoclimatic reconstructions, *Quaternary Sci. Rev.*, **35**, 1–22 (2012).

28. Ashe, E. L., et al. Statistical modeling of rates and trends in Holocene relative sea level, *Quaternary Sci. Rev.*, **204**, 58–77 (2019).

29. Sheinbaum, J. et al. Flow structure and transport in the Yucatan Channel, *Geophys. Res. Lett.*, **29**, 1040 (2002).

30. Jones, P. D., T. Jonsson, and D. Wheeler. Extension to the North Atlantic Oscillation Using Early Instrumental Pressure Observations from Gibraltar and South-West Iceland, *Int. J. Climatol.*, **17**, 1433–1450 (1997).

31. DiNezio, P. N., et al. Observed Interannual Variability of the Florida Current: Wind Forcing and the North Atlantic Oscillation, *J. Phys. Oceanogr.*, **39**, 721–736 (2009).

32. Enfield, D. B., et al. The Atlantic multidecadal oscillation and its relation to rainfall and river flows in the continental U.S., *Geophys. Res. Lett.*, **28**, 2077–2080 (2001)

33. Bingham, R. J., and C. W. Hughes. Signature of the Atlantic meridional overturning circulation in sea level along the east coast of North America, *Geophys. Res. Lett.*, **36**, L02603 (2009).

34. Little, C. M., et al. The Relationship between United States East Coast Sea Level and the Atlantic Meridional Overturning Circulation: a Review, *J. Geophys. Res.-Oceans*, **124**, 6435–6458 (2019).

35. Leaman, K. D., R. L. Molinari, and P. S. Vertes. Structure and Variability of the Florida Current at 27°N: April 1982–July 1984, *J. Phys. Oceanogr.*, **17**, 565–583 (1987).

36. Giese, B. S., and S. Ray. El Niõ variability in simple ocean data assimilation (SODA), 1871–2008, *J. Geophys. Res.*, **116**, C02024 (2011).

37. Santamaría-Gómez, A., et al. Uncertainty of the 20th century sea-level rise due to vertical land motion errors, *Earth Planet. Sci. Lett.*, **473**, 24–32 (2017).

38. Khan, N. S., et al. Drivers of Holocene sea-level change in the Caribbean, *Quaternary Sci. Rev.*, **155**, 13–36 (2017).

39. Love, R., et al. The contribution of glacial isostatic adjustment to projections of sea-level change along the Atlantic and Gulf coasts of North America, *Earth's Future*, **4**, 440–464 (2016).

40. Birol, F., et al. Coastal applications from nadir altimetry: Example of the X-TRACK regional products, *Adv. Space Res.*, **59**, 936–953 (2017).

41. Theiler, J., et al. Testing for nonlinearity in time series: the method of surrogate data, *Physica D*, **58**, 77–94 (1992).

42. Compo, G. P., et al. The Twentieth Century Reanalysis Project, *Q. J. R. Meteorol. Soc.*, **37**, 1–28 (2011).

43. Poli, P., et al. ERA-20C: An Atmospheric Reanalysis of the Twentieth Century, *J. Clim.*, **29**, 4083–4097 (2016).

44. Gray, A. R., and S. C. Riser. A Global Analysis of Sverdrup Balance Using Absolute Geostrophic Velocities from Argo, *J. Phys. Oceanogr.*, **44**, 1213–1229 (2014).

45. Drijfhout, S., et al. Is a Decline of AMOC Causing the Warming Hole above the North Atlantic in Observed and Modeled Warming Patterns?, *J. Clim.*, **25**, 8373–8379 (2012).

46. Roberts, C. D., F. K. Garry, and L. C. Jackson. A Multimodel Study of Sea Surface Temperature and Subsurface Density Fingerprints of the Atlantic Meridional Overturning Circulation, *J. Clim.*, **26**, 9155–9174 (2013).

47. Rayner, N. A., et al. Global analyses of sea surface temperature, sea ice, and night marine air temperature since the late nineteenth century, *J. Geophys. Res.*, **108**, 4407 (2003).

48. Kaplan, A., et al. Analyses of global sea surface temperature 1856–1991, *J. Geophys. Res.*, **103**, 18567–18589 (1998).

49. Gulev, S. K., M. Latif, N. Keenlyside, W. Park, and K. P. Koltermann. North Atlantic Ocean control on surface heat flux on multidecadal timescales, *Nature*, **499**, 464–467 (2013).

50. Lumpkin, R., and G. C. Johnson. Global ocean surface velocities from drifters: Mean, variance, El Niño-Southern Oscillation response, and seasonal cycle, *J. Geophys. Res.-Oceans*, **118**, 2992–3006 (2013).

Supplementary Information is linked to the online version of the paper at www.nature.com/nature.

Acknowledgements Funding came from NSF awards OCE-1558966 and OCE-1834739. I acknowledge helpful conversations with M. Andres, L. Beal, S. Coats, S. Elipot, N. Foukal, G. Gawarkiewicz, J. Gebbie, J. Heiderich, Y.-O. Kwon, C. Little, and S. Wijffels.

Author Contributions C.G.P. conceived the study, formulated the model framework, performed the analyses, and wrote the manuscript.

Competing Interests The author declares that they have no competing financial interests.

Correspondence Correspondence and requests should be addressed to C.G.P. (cpiecuch@whoi.edu).

Data Availability The tide gauge data and submarine cable data that support the main findings of this study are available from the Permanent Service for Mean Sea Level (PSMSL; http://www.psmsl.org/) and the National Oceanic and Atmospheric Administration Atlantic Oceanographic and Meteorological Laboratory (NOAA AOML; https://www.aoml.noaa.gov/), respectively. Ancillary data sets, used for interpretation and not incorporated into the Bayesian model, and their availabilities are as follows: Surface drifter data of surface current speeds shown in Figure 1a are available from NOAA AOML; Global Digital Elevation Model bathymetry shown in Figures 1b and 4 are available from NOAA National Geophysical Data Center (NGDC; https://www.ngdc.noaa.gov/); Cruise data from the R/V Walton Smith shown in Figure 4 are available from NOAA AOML; Reanalysis wind-stress fields shown in Figure 5 are available from the Woods Hole Oceanographic Institution Community Storage Server (WHOI CCS; https://cmip5.whoi.edu); Gridded data sets of sea-surface temperature shown in Figure 6 are available from the WHOI CCS, UK Met Office Hadley Centre (https://www.metoffice.gov.uk/hadobs/), and NOAA Earth System Research Laboratory Physical Sciences Division (ESRL PSD; https://www.esrl.noaa.gov/psd/); Time series of climate indices shown in Supplementary Figure 2 are available from NOAA ESRL PSD; Global Positioning System data of vertical land motion rates shown in Supplementary Table 1 are available from Système d'Observation du

Niveau des Eaux Littorales (SONEL; http://www.sonel.org/); Proxy relative sea-level index points shown in Supplementary Table 2 are taken from Khan et al.[38] and Love et al.[39]; Satellite-altimetric time series of sea-surface height shown in Supplementary Figure 6 are available from Centre of Topography of the Oceans and the Hydrosphere (CTOH; http://http://ctoh.legos.obs-mip.fr/); Model estimates of glacial isostatic adjustment rates used in the synthetic data experiments are available from PSMSL; Global-mean thermosteric sea level from the Community Climate System Model Version 4 used in the synthetic data experiments was downloaded from the WHOI CCS; Model solutions from the Simple Ocean Data Experiment (SODA) shown in Supplementary Figures 4, 15 and used in the synthetic data experiments are available from the University of Hawaii Asia-Pacific Data-Research Center (http://apdrc.soest.hawaii.edu/). Maps in display items were produced using the Mapping Toolbox in MATLAB.

Code Availability Statement The computer code used to run the Bayesian model and produce the results in this study, written in the MATLAB software environment, is available at the corresponding author's GitHub website (https://github.com/christopherpiecuch).

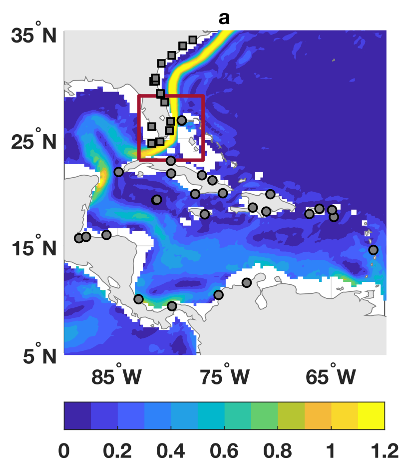
a
b
35°N
25°N
15°N
5°N
85°W
75°W
65°W
0
0.2
0.4
0.6
0.8
1
1.2
29°N
27°N
25°N
23°N
82°W
80°W
78°W
-1000
-800
-600
-400
-200
0
Grand Bahama
West Palm Beach
NW Providence
Miami
Bimini
Cat Cays
Key West
Santaren
Yucatan
Cay Sal Bank
Nicholas
Havana

402 [Fig. 1]

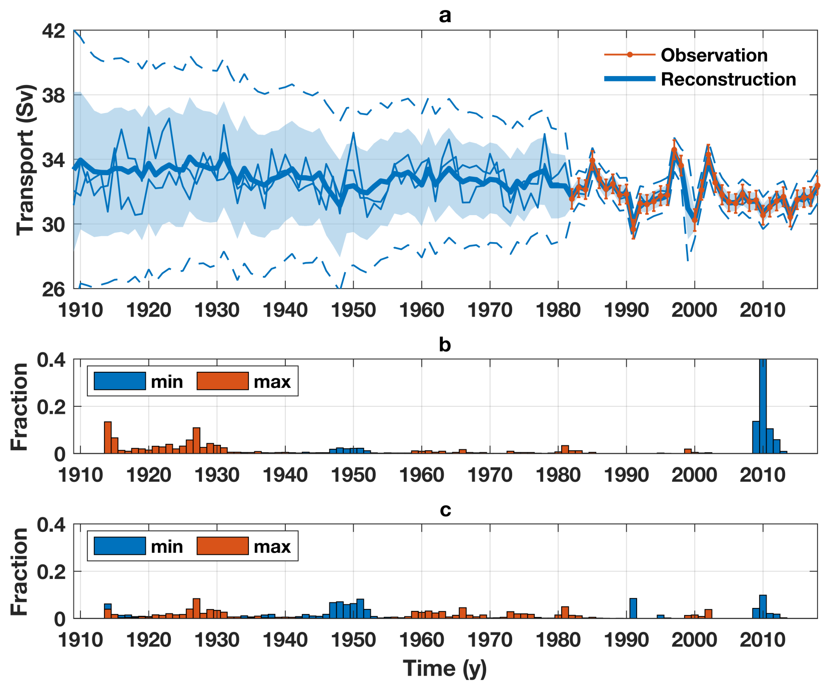
a
Observation
Reconstruction
Transport (Sv)
42
38
34
30
26
1910
1920
1930
1940
1950
1960
1970
1980
1990
2000
2010
b
Fraction
0.4
0.2
0
min
max
c
Fraction
min
max
Time (y)

403 [Fig. 2]

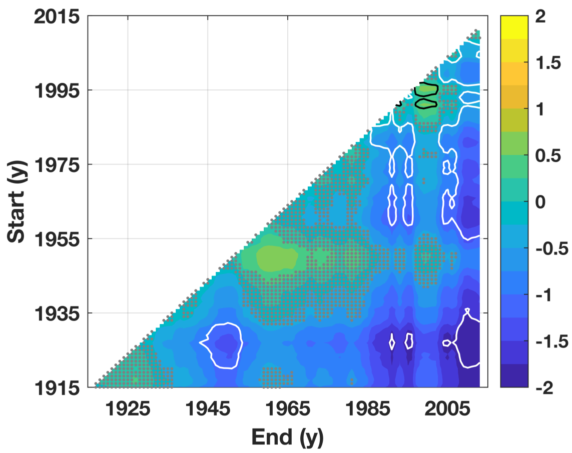

2015
1995
1975
1955
1935
1915
Start (y)
1925
1945
1965
1985
2005
End (y)
2
1.5
1
0.5
0
-0.5
-1
-1.5
-2

[Fig. 3]

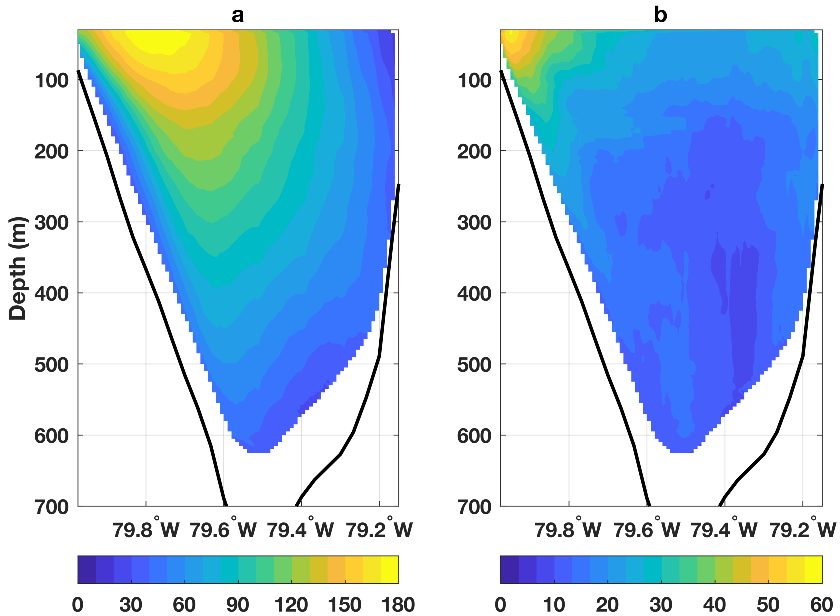
a
b
Depth (m)
100
200
300
400
500
600
700
79.8°W
79.6°W
79.4°W
79.2°W
0
30
60
90
120
150
180
0
10
20
30
40
50
60

[Fig. 4]

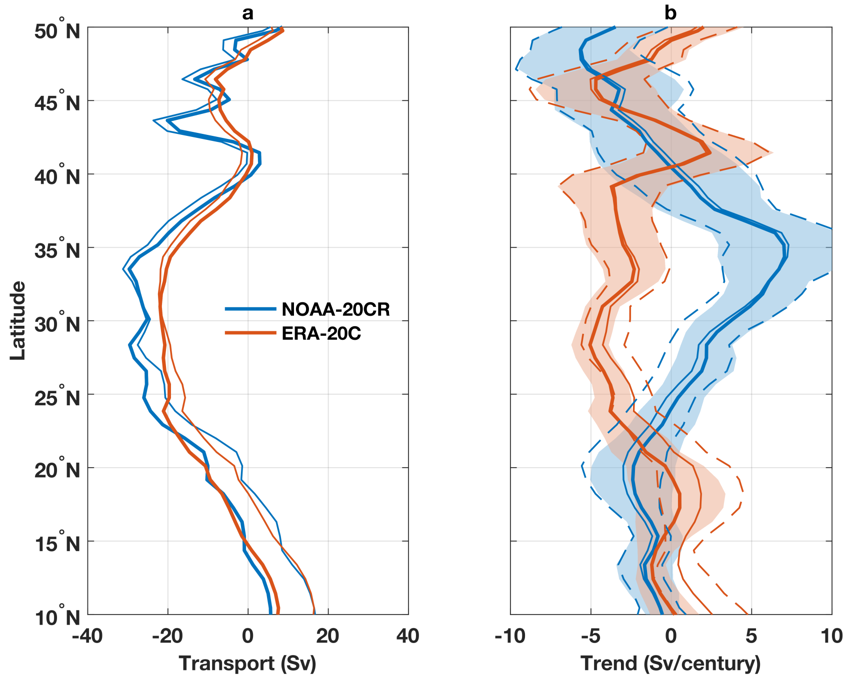

a
b
50°N
45°N
40°N
35°N
30°N
25°N
20°N
15°N
10°N
Latitude
-40
-20
0
20
40
Transport (Sv)
NOAA-20CR
ERA-20C
-10
-5
0
5
10
Trend (Sv/century)

406 [Fig. 5]

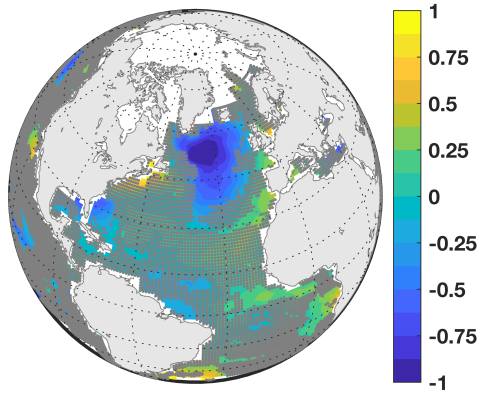

407 [Fig. 6]

Methods

Observational data used in the Bayesian model I use annual relative sea level from 46 tide gauges in the southeastern USA (19 records), Caribbean Islands (20 records), southeastern Central America (5 records), and northern South America (2 records) during 1909–2018 (Figure 1a; Supplementary Figure 7; Supplementary Table 3). Data were downloaded from the Permanent Service for Mean Sea Level (PSMSL) Revised Local Reference (RLR) database[26] on 4 February 2019. The study period is the longest interval such that, for each year, data is available from at least one southeastern USA tide gauge and at least one gauge in the Caribbean Islands, southeastern Central America, or northern South America. Over the study period, each tide gauge returns on average ~ 30 y of data, but some have as few as ~ 10 y of data, whereas others have as many as ~ 100 y. The time series together constitute 1,390 y of data over the study period ($\sim 27\%$ completeness).

I also use Florida Current transport from submarine telephone cables at 27°N between West Palm Beach and Grand Bahama (Figure 1b)[1–4]. Using electromagnetic theory, changes in the flow can be estimated from voltages induced across the cable due to the transport of charged particles by the variable current[3]. The original cable spanned from Jupiter Inlet to Settlement Point, giving measurements from 18 March 1982 to 22 October 1998; observations resumed on 19 June 2000 based on a cable running from West Palm Beach to Eight Mile Rock (Figure 1b). Transports are provided by the National Oceanic and Atmospheric Administration (NOAA) at 1-day intervals, but the data have an effective sampling rate of 3 days, due to low-pass filtering applied to the original observations. I use annual averages of the daily data (Figure 2a). Given a standard error of 1.7 Sv on the daily values[4], I estimate standard errors on the annual averages of 0.30–0.35 Sv, depending on data availability in any given year, consistent with values computed by Garcia and Meinen[4].

Bayesian framework

I apply a hierarchical dynamical spatiotemporal model[27,28,51,52] to the submarine-cable data and tide-gauge records to infer annual changes in Florida Current transport and coastal sea level. The model comprises three levels: a process level describing how the quantities of interest relate to one another, and vary in space and time; a data level specifying how the imperfect available data correspond to the quantities of interest; and a parameter level placing prior constraints on the uncertain parameters in the process and data levels. My model builds on the Bayesian algorithm of Piecuch et al.[53], who studied the origin of spatial variation in sea-level trends on the east coast of the USA during 1900–2017. Here I develop new equations to consider an expanded geographic region, incorporate the submarine-cable data, and represent the relationship between Florida Current transport and the difference in coastal sea level across the Florida Straits. See the Supplementary Information for residual analyses and synthetic data experiments that establish the appropriateness of the model given the data, and exemplify its ability to accurately estimate the quantities of interest given the available incomplete, noisy, biased data.

Process level

Coastal sea level Coastal relative sea level is a process with spatiotemporal covariance[54,55]. As in Piecuch et al.[53], I model sea level, $\boldsymbol{\eta}_k = [\eta_{1,k}, \ldots, \eta_{N,k}]^{\mathsf{T}}$, at steps $k \in \{1, \ldots, K\}$ and sites $n \in \{1, \ldots, N\}$, as the sum of a spatially correlated autoregressive process of order 1 and a large-scale spatial field of linear temporal trends,

$$\boldsymbol{\eta}_k - \boldsymbol{b}t_k = r\left(\boldsymbol{\eta}_{k-1} - \boldsymbol{b}t_{k-1}\right) + \boldsymbol{e}_k. \tag{1}$$

In Eq. (1), t_k is the time at step k, r is the lag-1 autocorrelation coefficient, $\boldsymbol{b}$ is the spatial vector of temporal trends, and $\boldsymbol{e}_k$ is an innovation sequence driving the autoregressive process. Supplementary Table 4 describes all of the model parameters. I set $\sum_{k=1}^{K} t_k = 0$ to represent $\boldsymbol{\eta}_k$ as anomalies from a time mean. The trend vector $\boldsymbol{b}$ is modeled as a random normal field with spatial structure, $\boldsymbol{b} \sim \mathcal{N}\left(\mu \mathbf{1}_N, \mathsf{\Pi}\right)$, such that μ is the spatial mean, $\mathbf{1}_X$ is a $X \times 1$ column vector of ones, and,

$$\mathsf{\Pi}_{ij} = \pi^2 \exp\left(-\lambda \left|\mathbf{s}_i - \mathbf{s}_j\right|\right). \tag{2}$$

Here π^2 is the partial sill, λ is the inverse range, and $|\mathbf{s}_i - \mathbf{s}_j|$ is distance between target sites $\mathbf{s}_i$ and $\mathbf{s}_j$. The symbol $\sim$ means "is distributed as" and $\mathcal{N}\left(\boldsymbol{p}, \mathsf{q}\right)$ is the multivariate normal distribution with mean vector $\boldsymbol{p}$ and covariance matrix q.

I cast $\boldsymbol{e}_k$ as a temporally independent, identically distributed (iid), but spatially correlated vector with zero mean, $\boldsymbol{e}_k \sim \mathcal{N}\left(\mathbf{0}_N, \Sigma\right)$, where $\mathbf{0}_X$ is a $X \times 1$ column vector of zeros, and,

$$\Sigma_{ij} = \left(\mathsf{c}_{ij}\right) \sigma^2 \exp\left(-\phi \left|\mathbf{s}_i - \mathbf{s}_j\right|\right). \tag{3}$$

Here σ^2 is the partial sill and ϕ is the inverse range. Matrix element $\mathsf{c}_{ij} = 1$ if locations $\mathbf{s}_i$ and $\mathbf{s}_j$ are either both on the southeastern USA or both along the Caribbean, Central America, or

South America. Otherwise, $\mathsf{c}_{ij} = 0$. That is, sea level covaries within, but not between, these regions. This spatial covariance structure is motivated by previous analyses of tide-gauge records and satellite-altimetry data. Thompson and Mitchum[56] applied clustering methods to low-pass-filtered tide-gauge records during 1952–2001, finding that the Caribbean Sea (which in their analysis comprised Cuba, Puerto Rico, and Colombia) formed one cluster of coherent sea-level variation, and the southeastern USA (from Florida to North Carolina) formed another cluster. Zhao and Johns[57] determined that Florida Current transports over 1993–2011 were positively correlated with sea-surface height over the Caribbean Sea (including the Bahamas) and along southeastern Central America, but negatively correlated with sea-surface height on the southeastern USA coast on interannual timescales.

Florida Current transport For periods longer than a day, the momentum balance across Florida Straights will be nearly geostrophic. Assuming that subsurface pressure signals are vertically coherent[33,34], variations in Florida Current transport should therefore be correlated with changes in the sea-level difference across Florida Straits. Based on this reasoning, I assume that the relationship between annual Florida Current transport, $\boldsymbol{T} = [T_1, \ldots, T_K]^\mathsf{T}$, and coastal sea level, $\eta = [\boldsymbol{\eta}_1, \ldots, \boldsymbol{\eta}_K]$, at times $\boldsymbol{t} = [t_1, \ldots, t_K]^\mathsf{T}$ can be written as,

$$\boldsymbol{T} = \overline{T}\mathbf{1}_K + \rho\eta^\mathsf{T}\boldsymbol{\Delta} + \alpha\boldsymbol{t} + \boldsymbol{w}. \tag{4}$$

Here $\overline{T}$ is the time-mean transport and ρ is a scalar coefficient representing the change in transport per unit change in sea-level difference across the Florida Straits. I assume that ρ is a constant, and does not vary with time period or frequency band. While it might appear simplistic, this assumption is justified based on admittance and coherence analysis applied to output from an ocean general circulation model (see Supplementary Information). The $N \times 1$ vector $\boldsymbol{\Delta}$ is a differencing operator, such that $\Delta_i = 1$ if site i is Settlement Point (the tide gauge nearest to the eastern end of the submarine cable in the Bahamas), $\Delta_i = -1$ if site i is West Palm Beach (the closest tide gauge to the western end of the cable in southeastern Florida), and zero otherwise. Hence, $\rho\eta^{\mathsf{T}}\boldsymbol{\Delta}$ is the sea-level difference across Florida Straits converted into units of a transport.

The remaining terms in Eq. (4) account for other effects unrelated to large-scale geostrophic ocean dynamics. The scalar α represents an apparent trend in $\boldsymbol{T}$, included to correct for longterm static sea-level changes unrelated to ocean dynamics, for example, due to glacial static adjustment[25]. That is, $\boldsymbol{b}^{\mathsf{T}}\boldsymbol{\Delta}$ is the difference in sea-level trends across Florida Straits, resulting from both dynamic processes and static effects. Hence, in Eq. (4), $\boldsymbol{b}^{\mathsf{T}}\boldsymbol{\Delta} + \alpha/\rho$ represents the dynamic component of the difference in sea-level trends across Florida Current, and $-\alpha/\rho$ constitutes the static component of the trend in sea-level differences across the Florida Straits (Supplementary Figure S3). Satellite altimetry, GPS data, and proxy sea-level index points support this interpretation of Eq. (4) (cf. the Main Text). I also include $\boldsymbol{w} = [w_1, \ldots, w_K]^{\mathsf{T}}$, which is modeled as iid uncorrelated white noise, $w_k \sim \mathcal{N}(0, \omega^2)$, with variance ω^2, to parameterize the response to local atmospheric or terrestrial forcing, such as river runoff, air pressure, or wind stress across Florida Straits.

Data level

Tide-gauge records Following Piecuch et al.[53], I represent annual data from tide gauges, $\boldsymbol{z}_k = [z_{1,k}, \ldots, z_{M_k,k}]^{\mathsf{T}}$, at $M_k \leq N$ locations at time step k, as corrupted (incomplete, noisy, biased) versions of the underlying $\boldsymbol{\eta}_k$ process,

$$\boldsymbol{z}_k = \mathsf{H}_k \boldsymbol{\eta}_k + \boldsymbol{d}_k + \mathsf{F}_k \left(\boldsymbol{a} t_k + \boldsymbol{\ell} \right). \tag{5}$$

Here $\boldsymbol{d}_k$ is a random error sequence, which is modeled as a spatially and temporally uncorrelated normal field, $\boldsymbol{d}_k \sim \mathcal{N}\left(\mathbf{0}_{M_k}, \delta^2 \mathsf{I}_{M_k}\right)$, with variance δ^2. A vector of location-specific offsets $\boldsymbol{\ell}$ are imposed and represented as a spatially uncorrelated Gaussian field, $\boldsymbol{\ell} \sim \mathcal{N}\left(\nu \mathbf{1}_M, \tau^2 \mathsf{I}_M\right)$, with mean ν, variance τ^2, and where M is the number of tide gauges, such that $N \geq M \geq M_k \; \forall k$. Purely local error trends in the data $\boldsymbol{a}$ are also modeled as a random normal field without spatial correlation, $\boldsymbol{a} \sim \mathcal{N}\left(\mathbf{0}_M, \gamma^2 \mathsf{I}_M\right)$, with variance γ^2. Finally, H_k and F_k are selection matrices, filled with zeros and ones, which pick out $\boldsymbol{\eta}_k$, $\boldsymbol{a}$, or $\boldsymbol{\ell}$ values at the observation sites for time t_k.

Submarine-cable measurements I assume that L annual data values from the submarine cable, $\boldsymbol{x} = [x_1, \ldots, x_L]^{\mathsf{T}}$, are available and represent imperfect (incomplete and noisy) versions of the underlying $\boldsymbol{T}$ process,

$$\boldsymbol{x} = \mathsf{G} \boldsymbol{T} + \boldsymbol{u}. \tag{6}$$

Here G is a $L \times K$ selection matrix, picking out years when cable data are available, and $\boldsymbol{u} = [u_1, \ldots, u_L]^{\mathsf{T}}$ is a zero-mean random data error sequence, $u_l \sim \mathcal{N}\left(0, \xi_l^2\right)$, where the ξ_l^2 are set equal to the corresponding submarine-cable data standard error variances mentioned above and computed based on the availability of data in any given year.

Parameter level To close the model, priors are placed on the parameters in the process- and data-level equations. Similar to Piecuch et al.[53], I use proper, mostly conjugate prior forms. Prior forms and hyperparameter values are given in Supplementary Table 5. The selection of the hyper-parameter values follows the basic logic in Piecuch et al.[53]. My philosophy is to employ diffuse and uninformative priors. To quantify the importance of priors relative to the data, after I compute the posterior solutions (see immediately below), I compare widths of the 95% credible intervals from the posterior and prior probability distribution functions for each parameter (Supplementary Table 6). If prior and posterior credible intervals have similar widths, then the posterior solutions are largely determined by the prior assumptions. If posterior credible intervals are much narrower than the prior credible intervals, then the posterior solutions are mostly constrained by the observations. Almost universally, the 95% posterior credible intervals are much narrower than the 95% prior credible intervals (Supplementary Table 6), implying that posterior inference is drawn predominantly from the information content of the observations, and not overly influenced by prior beliefs encoded into the model.

Drawing samples from the posterior distribution Given the model equations, I use Bayes' rule, and assume that the posterior probability distribution function takes the form,

$$
\begin{aligned}
p\left(\eta, \boldsymbol{T}, \Theta | \mathbf{Z}, \boldsymbol{x}\right) &\propto p\left(\mathbf{Z}, \boldsymbol{x} | \eta, \boldsymbol{T}, \Theta\right) \times p\left(\eta, \boldsymbol{T} | \Theta\right) \times p\left(\Theta\right) \\
&= p\left(\boldsymbol{\eta}_0\right) \times p\left(\overline{T}\right) \times p\left(r\right) \times p\left(\sigma^2\right) \times p\left(\phi\right) \times p\left(\mu\right) \times p\left(\pi^2\right) \\
&\times p\left(\lambda\right) \times p\left(\delta^2\right) \times p\left(\nu\right) \times p\left(\tau^2\right) \times p\left(\gamma^2\right) \times p\left(\rho\right) \times p\left(\alpha\right) \\
&\times p\left(\omega^2\right) \times p\left(\boldsymbol{b} | \mu, \pi^2, \lambda\right) \times p\left(\boldsymbol{\ell} | \nu, \tau^2\right) \times p\left(\boldsymbol{a} | \gamma^2\right) \times p\left(\boldsymbol{x} | \boldsymbol{T}\right) \\
&\times p\left(\boldsymbol{T} | \eta, \rho, \alpha, \omega^2, \overline{T}\right) \times \prod_{k=1}^{K} \left[p\left(\boldsymbol{z}_k | \boldsymbol{\eta}_k, \boldsymbol{a}, \boldsymbol{\ell}, \delta^2\right) \times p\left(\boldsymbol{\eta}_k | \boldsymbol{\eta}_{k-1}, \boldsymbol{b}, r, \sigma^2, \phi\right)\right]
\end{aligned}
\tag{7}
$$

In Eq. (7), $\mathbf{Z}$ is the structure of all tide-gauge data points, p is used to represent probability distribution function, $|$ is conditionality, $\propto$ is proportionality, and $\Theta \doteq \{r, \sigma^2, \phi, \dots\}$ is used to represent the set of all model parameters. I assume that the observations are conditionally independent, provided the process and parameters.

Draws from the posterior probability distribution function are made as in Piecuch et al.[53]. I use Markov chain Monte Carlo (MCMC) methods, evaluating the full conditional distributions for process and parameter values using a Gibbs sampler, but using Metropolis steps for the inverse range parameters. I run 200,000 MCMC iterations, setting initial process values to zero, and drawing initial parameter values randomly from the respective prior distribution. To remove initialization transients, I discard the first 100,000 iterations as burn in, and then I keep only 1 out of every 100 of the remaining 100,000 iterations to reduce serial correlation effects between draws. Results shown here are based on a 3,000-element chain produced by performing the above procedure 3 times and stitching together the resulting 1,000-member chains. Solutions for scalar parameters are summarized in Supplementary Table 6. To evaluate convergence of the solution for each parameter, I compute the convergence monitor $\hat{R}$ of Gelman and Rubin[58], which compares the variance within and between the 3 different 1,000-member solutions. In each case, $\hat{R} \sim 1.00$ (Supplementary Table 6), indicating that the solutions have converged.

Local and global uncertainty measures

The probabilistic nature of the model solutions allows for the calculation of both pointwise and pathwise uncertainty measures[59]. Pointwise statistics measure probabilities locally. The light blue shading in Figure 2a represents the 95% pointwise posterior credible intervals computed from the transport solutions at each year of the reconstruction. The interpretation is that, for each year, there is a 95% chance that the true transport value falls within this blue shading.

Pathwise statistics measure probabilities more globally. The dashed blue lines in Figure 2a represent the 95% pathwise posterior credible intervals calculated from the transport estimates across all years of the reconstruction. These values are computed by widening the 95% pointwise posterior credible intervals until 95% of modeled transport time series are captured in their entirety. That is, there is a 95% chance that the full time series of transport does not stray outside the bounds of these pathwise credible intervals.

Other examples of pathwise statistics include values quoted in the text for the minimum and maximum decadal-average transports and the corresponding histograms of their timing shown Figure 2b, 2c. For each of the 3,000 ensemble members comprising the posterior solution, I smooth the transport time series using an 11-point boxcar window, and then identify the minimum and maximum transport values along with the times at which they occurred. These values vary from one ensemble member to the next, and so performing this procedure for each ensemble member allows me to populate histograms for the transport extrema and their occurrence times.

Hypothesis testing

In addition to generating posterior solutions for transport and sea level, the Bayesian model provides data-constrained estimates of the various model parameters (e.g., Supplementary Table 6). This allows for rigorous hypothesis testing through simulation experiments. For example, in Figure 3, I show the change in decadal-average Florida Current transport between all possible pairs of decades, and indicate the probability that such changes would have occurred given a stationary red-noise process with the same autocorrelation and variance characteristics. As a specific instance, I state that decadally averaged transport declined by 1.2 ± 1.2 Sv from 1970–1980 to the present, and that this decline is extremely likely (probability $P = 0.96$) more than would be expected from stationary red noise. This conclusion was determined as follows. First, I use the posterior transport solutions to compute a histogram of transport averaged over 2008–2018 minus the transport averaged over 1970–1980. Next, I use the posterior solutions for the scalar model parameters as the basis for the simulation of a parallel set of 3,000 synthetic transport time series following Eqs. (1) and (4) but with the trends ($\boldsymbol{b}$ and α) set to zero. Then, I populate histograms of the difference between decadally averaged synthetic transport between 1970–1980 and 2008–2018. Finally, I compute what fraction of the original posterior transport solutions shows more of a decline than is shown by the stationary synthetic transport process, which, in this example case, is 0.96.

51. Cressie, N., & C. K. Wikle. Statistics for Spatio-Temporal Data, John Wiley & Sons, 588 pp (2011).

52. Banerjee, S., B. P. Carlin, & A. E. Gelfand. Hierarchical Modeling and Analysis for Spatial Data, Chapman and Hall, Boca Raton, 448 pp (2004).

53. Piecuch, C. G., et al. Origin of spatial variation in US East Coast sea-level trends during 1900–2017, *Nature*, **564**, 400–404 (2018).

54. Bos, M. S., S. D. P. Williams, I. B. Araújo, & L. Bastos. The effect of temporal correlated noise on the sea level rate and acceleration uncertainty, *Geophys. J. Int.*, **196**, 1423–1430.

55. Hughes, C. W., and M. P. Meredith. Coherent sea-level fluctuations along the global continental slope, *Phil. Trans. R. Soc. A.*, **364**, 885–901 (2006).

56. Thompson, P. R., and G. T. Mitchum. Coherent sea level variability on the North Atlantic western boundary, *J. Geophys. Res. Oceans*, **119**, 5676–5689, doi:10.1002/2014JC009999 (2014).

57. Zhao, J., and W. Johns. Wind-forced interannual variability of the Atlantic Meridional Overturning Circulation at $26.5°$N, *J. Geophys. Res.-Oceans*, **119**, 2403–2419.

58. Gelman, A., and D. B. Rubin. Inference from iterative simulation using multiple sequences, *Stat. Sci.*, **7**, 457–472 (1992).

59. Tingley, M. P., & P. Huybers. Recent temperature extremes at high northern latitudes unprecedented in the past 600 years, *Nature*, **496**, 201–205 (2013).

Figure 1 **Florida Current and study region.** **a,** Gray squares (circles) are locations of tide gauges in the southeastern USA (Caribbean). Shading is mean ocean surface current speed (m s^{-1}) from surface-drifter data[50]. Red box is area shown in (b). **b,** Details of Florida Straits. Shading is ocean depth (m). Bold (light oblique) font indicates ocean channels (land locations) mentioned in the text. Thick red lines are locations of submarine cable measurements. Thin purple lines are locations of *in situ* measurements from past studies[13–16].

Figure 2 **Florida Current transport.** **a,** Blue shows posterior median (thick line), 95% pointwise (light shading) and pathwise (dash dot) credible intervals, and two arbitrary ensemble members (thin lines) from the probabilistic Florida Current transport solution. Orange shows annual transport from raw submarine cable data plus and minus twice the standard error[2]. **b,** Histograms of modeled probabilities that the minimum (blue) and maximum (orange) decadal average transport occurred centered on a given year. **c,** As in (b) but histograms were calculated after having removed the corresponding longterm trend. See Methods for discussion of statistics and uncertainty measures.

Figure 3 **Weakening of Florida Current transport over different periods.** Shading shows posterior median estimates of the change in decadal-average Florida Current transport between all pairs of decades (Sv). Negative values indicate that transport fell from the start to the end decade. Stippling indicates that it is as likely as not ($0.33 < P < 0.67$) that transport rose or fell. White (black) contours encircle periods when it is very likely

($P > 0.90$) that transport weakened (strengthened) from the start to the end decade more than expected from a stationary red noise process (see Methods for discussion of calculations of significance).

Figure 4 **Structure of the Florida Current within Florida Straits.** **a,** Mean northward velocities (m s^{-1}) through Florida Straits from shipboard acoustic doppler current profiler data from 70 research cruises of the R/V Walton Smith between 2001–2018. Values are computed by interpolating all data between $26.9°$N and $27.1°$N from a given cruise onto a common grid, and then averaging over all cruises. For a value to be shown at a longitude and depth, data must have been available from at least 14 cruises. **b,** As in (a) but showing the standard deviation in meridional velocities (m s^{-1}) across cruises.

Figure 5 **Changes in wind-stress curl and gyre circulation.** **a,** Thick lines are time-mean geostrophic Sverdrup streamfunction[6] computed from wind-stress curl from NOAA 20CR[42] and ERA 20C[43] reanalyses over 1900–2010 as a function of latitude in the North Atlantic. Thin lines are the same, but also incorporate the ageostrophic Ekman transport integrated across the basin. **b,** Median estimates (thick lines) and formal 95% confidence intervals (colored shading) of the trend in Sverdrup streamfunction versus latitude during 1900–2010 from the two reanalyses. Thin and dashed lines represent median estimates and confidence intervals, respectively, with Ekman transports included.

Figure 6 **Changes in sea-surface temperature.** Shaded values are sea-surface temperature trends (°C century^{-1}) since 1909 averaged over three products: ERA-20C[43], HadISST[47], and Kaplan[48]. Stippling indicates that the magnitude of the average trend is less than 2.35 (the $P = 0.95$-value of the inverse t-distribution for 3 degrees of freedom) times the sample standard deviation computed across the three different products at a given grid cell, and is meant as a rough indicator of where values are not significant.

Supplementary Information for "Weakening of the Gulf Stream at Florida Straits over the past century inferred from coastal sea-level data"

Christopher G. Piecuch[1]

[1] *Woods Hole Oceanographic Institution, Woods Hole, Massachusetts, USA*

S1 Heat budget

Previous studies interpret a "warming hole" over the subpolar North Atlantic Ocean, where surface temperatures have cooled relative to the global mean over the past century (Figure 6), in terms of a slowing deep Atlantic meridional overturning circulation[1–3]. These interpretations are partly based on regression analyses of climate-model output, which suggest that, for every 1-Sv decline in the deep overturning, subpolar sea-surface temperatures cool by 0.2–0.6°C[1,2,4,5].

To assess whether observed cooling of the subpolar-Atlantic sea surface and hypothesized slowdown of the deep overturning circulation are consistent with my independent determination of a weakening Florida Current transport, I formulate simple ocean heat budget. The control volume is taken to be the full-depth Atlantic Ocean north of 27°N. I ignore transports through Bering Strait, and changes in evaporation minus precipitation over the basin. I also assume that, on these space- and timescales, local heat storage is negligible to leading order (see below). Thus, the heat budget is a balance between heat transport divergence due to weakening of the Florida Current and deep overturning circulation at 27°N, and turbulent ocean heat gain at the surface due to cooling sea-surface temperatures in the subpolar region.

Following Marshall et al.[6], the volume-integrated ocean heat transport divergence $\mathcal{Q}_{moc}$ can be written as,

$$\mathcal{Q}_{moc} \doteq -\rho_o c_o \overline{\Delta T}^z \Psi, \tag{S1}$$

where $\rho_o = 1029$ kg m^{-3} is ocean water density, $c_o = 3994$ J kg^{-1} °C^{-1} is seawater's specific heat capacity, Ψ is the overturning streamfunction, and $\overline{\Delta T}^z$ is the temperature difference between the warm waters in Florida Straits and cool waters below ~ 1000 m over the open Atlantic Ocean.

The area-integrated turbulent heat gain at the surface $\mathcal{Q}_{surf}$ is expressed,

$$\mathcal{Q}_{surf} \doteq A\left(Q_E + Q_H\right), \tag{S2}$$

where A is the ocean surface area over which the heat gain occurs, and Q_E and Q_H are latent and sensible heat fluxes, respectively. After Large and Yeager[7], the turbulent heat fluxes are written as,

$$Q_E \doteq \Lambda_v \rho_a C_E \left[q\left(z_q\right) - q_{sat}\left(SST\right)\right]\left|\Delta\vec{U}\right|, \tag{S3}$$

and,

$$Q_H \doteq \rho_a c_a C_H \left[\theta\left(z_\theta\right) - SST\right]\left|\Delta\vec{U}\right|, \tag{S4}$$

where $\Lambda_v = 2.5 \times 10^6$ J kg^{-1} is the latent heat of vaporization, $\rho_o = 1.22$ kg m^{-3} is near-surface density of air, $c_a = 1000.5$ J kg^{-1} °C^{-1} is the specific heat capacity of air, $C_H \doteq 0.018\sqrt{C_D}$ (where C_D is the drag coefficient), $C_E \doteq 0.0346\sqrt{C_D}$, $q\left(z_q\right)$ and $\theta\left(z_\theta\right)$ are potential air temperature and specific humidity, respectively, $\left|\Delta\vec{U}\right|$ is surface wind speed, SST is sea-surface temperature, and,

$$q_{sat} \doteq \frac{q_1}{\rho_a} \exp\left(q_2 / SST\right), \tag{S5}$$

where $q_1 = 0.98 \times 640380$ kg m^{-3} and $q_2 = -5107.4$ K.

Using Eq. ($S5$) to linearize Eq. ($S3$) about a background sea-surface temperature $\overline{SST}$ gives,

$$Q_E = \Lambda_v \rho_a C_E \left[q\left(z_q\right) + \frac{q_2}{\overline{SST}^2} \left(SST - \overline{SST}\right) q_{sat}\left(\overline{SST}\right) \right] \left|\Delta\vec{U}\right|. \tag{S6}$$

Equating Q_{moc} and Q_{surf}, making use of Eqs. ($S4$) and ($S6$), and solving for SST yields,

$$SST = \frac{-\frac{\rho_o c_o \overline{\Delta T}^z \Psi}{A\left|\Delta\vec{U}\right|\rho_a} - c_a C_H \theta\left(z_\theta\right) - \Lambda_v C_E q\left(z_q\right) + \Lambda_v C_E \frac{q_2}{\overline{SST}} q_{sat}\left(\overline{SST}\right)}{\Lambda_v C_E \frac{q_2}{\overline{SST}^2} q_{sat}\left(\overline{SST}\right) - c_a C_H}. \tag{S7}$$

Finally, differentiating with respect to Ψ gives,

$$\frac{\partial SST}{\partial \Psi} = -\frac{\rho_o c_o \overline{\Delta T}^z}{A\left|\Delta\vec{U}\right|\rho_a \left[\Lambda_v C_E \frac{q_2}{\overline{SST}^2} q_{sat}\left(\overline{SST}\right) - c_a C_H\right]}. \tag{S8}$$

This expression represents the SST change expected for a unit Ψ change under this simple model.

To compute an estimate of $\partial SST / \partial \Psi$, I must choose appropriate values for the remaining parameters. I choose $A = 6.7 \times 10^{12}$ m^2, which represents the area of the shaded (unhatched) subpolar region of cooling shown in Figure 6. Based on a contemporary ocean state estimate[8], I use $C_D = 0.0011$ so $C_E = 0.0012$ and $C_H = 0.00061$, 6.5–11.5°C for $\overline{SST}$, and 7.5–10.5 m s^{-1} for $\left|\Delta\vec{U}\right|$ as reasonable values for the subpolar Atlantic. I also use 10–15°C as a range for $\overline{\Delta T}^z$ judging from that same ocean state estimate. These parameter choices lead to an estimated range for $\partial SST / \partial \Psi$ of 0.3–0.6°C Sv^{-1}. This range is consistent with values of 0.2–0.5°C Sv^{-1} found by dividing the observed sea-surface-temperature trends across the subpolar gyre (Figure 6) by the model's posterior median estimate of the trend in Florida Current transport during the past century (Supplementary Figure 1b). These values also agree with the values of 0.2–0.6°C Sv^{-1} published based on regression analyses of sea-surface temperature and Atlantic overturning streamfunction from climate models[1,2,4,5].

Ignoring local heat storage In the heat budget, I assumed that local heat storage is negligible. This assumption is based on a simple scaling argument. Suppose that, in contrast, changes in local heat storage are in fact important, and have similar magnitude to the change in ocean heat transport divergence. In this case I can consider the quasi-balance between local storage and advection,

$$\left| V \frac{\delta}{\delta t} \left(\frac{\delta \Theta}{\delta t} \right) \right| \approx \left| \overline{\Delta T}^{z} \frac{\delta \Psi}{\delta t} \right|, \tag{S9}$$

where $\delta\Theta/\delta t$ is the rate of change in ocean temperature averaged over the control region, V is the volume of the control region, and δt is a time increment. That is, $\delta\left(\delta\Theta/\delta t\right)$ is the change in local ocean heat storage rate required to balance the change in heat transport convergence or divergence due to a trend in Ψ over the study period. Rearranging to solve for $\delta\left(\delta\Theta/\delta t\right)$ gives,

$$\left| \delta \left(\frac{\delta \Theta}{\delta t} \right) \right| \approx \left| \frac{1}{V} \overline{\Delta T}^{z} \frac{\delta \Psi}{\delta t} \delta t \right|, \tag{S10}$$

I take $\overline{\Delta T}^{z} =$ 10–15°C as before, $\delta\Psi/\delta t = 1.7$ Sv century^{-1} (the magnitude of the posterior median model estimate of the centennial trend in Florida Current transport), and $\delta t = 100$ y. Now, if $V = 6.6\text{–}8.7\times10^{16}$ m^3 (the volume of the full-depth North Atlantic north of 27°N, depending on whether marginal seas are included), then $\delta\left(\delta\Theta/\delta t\right) \sim$ 0.6–1.2°C century^{-1}. In other words, for a change in the local heat storage rate to be comparable to the change in ocean heat transport divergence, there would need to be a change in centennial temperature trends averaged over the full-depth control region of this magnitude. If, instead, I take $V = 1.2$–1.9×10^{16} m^3 (the volume of the top 700 m in the northern North Atlantic), then the required change in centennial temperature trends becomes $\delta\left(\delta\Theta/\delta t\right) \sim 2.8$–$6.6$°C century^{-1}. Such magnitudes are substantially larger than estimated changes in large-scale temperature trends in the Atlantic over the 20th century compared to previous centuries[9]. So, I conclude that local heat storage, while possibly making higher-order contributions to the budget, can be neglected in this lowest-order-of-magnitude exercise.

S2 Residual analysis

Various residual terms appear in the Bayesian model equations (see Methods). When building the algorithm, I made certain assumptions regarding the spatial and temporal structures of these residuals. To test whether these assumptions are appropriate given the data, I undertake a residual analysis, using the model equations to solve for the sea-level innovations $\boldsymbol{e}_k$, tide-gauge errors $\boldsymbol{d}_k$, transport innovations w_k, cable-data errors $\boldsymbol{u}$, tide-gauge error trends $\boldsymbol{a}$ and tide-gauge data bias $\boldsymbol{\ell}$.

I made the assumption that $\boldsymbol{e}_k$, $\boldsymbol{d}_k$, w_k, and $\boldsymbol{u}$ behave as iid temporal white noise. If this assumption is reasonable, then the posterior solutions should look random in time. However, if systematic structure is present, it would mean that this assumption is inappropriate, and that the model is misspecified given the data. Time series of posterior $\boldsymbol{e}_k$ and $\boldsymbol{d}_k$ solutions are shown in Supplementary Figure 8a, 8b for an arbitrary target location, while model solutions for w_k and $\boldsymbol{u}$ are shown in Supplementary Figure 8c, 8d. These time series look random in time, and there are no obvious signs of autocorrelation. The amplitudes of $\boldsymbol{e}_k$, $\boldsymbol{d}_k$, and w_k variations are consistent with posterior solutions for the respective variance or partial sill parameters σ^2, δ^2, and ω^2 (Supplementary Table 6), and the magnitude of fluctuations in $\boldsymbol{u}$ is in keeping with the prior error variances placed on the submarine-cable data.

To be more thorough, I compute sample autocorrelation coefficients directly from the posterior solutions for $\boldsymbol{e}_k$, $\boldsymbol{d}_k$, w_k, and $\boldsymbol{u}$ across all space and time points. I compare those values to the autocorrelation coefficients expected theoretically for temporal white noise, given the same number of time steps. Supplementary Figure 9 compares the empirical and theoretical autocorrelation coefficients for time lags between 1 and 20 y. Values calculated empirically from the posterior solutions are consistent with the theoretically expected values. More quantitatively, 96%, 95%, 93%, and 95% of empirical autocorrelation coefficients computed respectively from $\boldsymbol{e}_k$, $\boldsymbol{d}_k$, w_k, and $\boldsymbol{u}$ are captured by the theoretical 95% confidence intervals.

In addition to being random in time, $\boldsymbol{e}_k$ and $\boldsymbol{d}_k$ are supposed to have spatially invariant amplitudes. In Supplementary Figure 10, I map median estimates of standard deviations computed empirically from the posterior model solutions of $\boldsymbol{e}_k$ and $\boldsymbol{d}_k$ at each tide-gauge location. While there is some higher-order spatial variation, these values are to lowest order fairly uniform and constant in space, and very similar to the posterior estimates of the partial sill σ^2 and variance parameter δ^2 (Supplementary Table 6).

Motivated by past studies[10,11], I assume that $\boldsymbol{e}_k$ is spatially structured, such that there is covariance between sites along the Caribbean, Central America, and South America, and between sites on the southeastern USA, but no covariance between these two broad regions. These assumptions are reflected in the block structure of the theoretical covariance matrix Σ shown in Supplementary Figure 11b computed from the posterior median solution for the partial sill σ^2 (Supplementary Table 6). This theoretical covariance matrix is very similar to the covariance matrix determined empirically by comparing all pairs of posterior solutions for $\boldsymbol{e}_k$ (Supplementary Figure 11a). Indeed, the Pearson correlation coefficient between the two matrices in Supplementary Figure 11 is 0.91, and the theoretical covariance matrix explains 82% of the variance in the empirical covariance matrix.

Finally, I consider residual spatial fields of the tide-gauge data biases $\boldsymbol{\ell} - \nu\mathbf{1}$ and error trends $\boldsymbol{a}$. According to the data-level Eq. (5) for the tide gauges, these two vectors should have zero mean, no spatial correlation, and spatial variances of τ^2 and γ^2, respectively. Supplementary Figure 12 facilitates an assessment of these assumptions, showing both posterior solutions for $\boldsymbol{\ell} - \nu\mathbf{1}$ and $\boldsymbol{a}$ as well as the solutions expected for a zero-mean random process given the posterior solutions for τ^2 and γ^2 (Supplementary Table 6). Consistent with model assumptions, these vector fields look fairly random, scattered about zero. The spatial spread in $\boldsymbol{\ell} - \nu\mathbf{1}$ and $\boldsymbol{a}$ appears consistent with the posterior τ^2 and γ^2 solutions. Indeed, 95% of the posterior $\boldsymbol{\ell} - \nu\mathbf{1}$ solutions are captured by the 95% credible intervals predicted for a zero-mean, spatially uncorrelated Gaussian process with variance τ^2, and similarly 95% of posterior solutions for $\boldsymbol{a}$ fall within the 95% credible interval produced by simulating a zero-mean random normal field with variance γ^2 (Supplementary Figure 12).

In conclusion, the design of my Bayesian algorithm is supported by residual analysis, which demonstrates that the model structure is appropriate and warranted given the available data.

S3 Sensitivity of model solutions to input data

Posterior solutions for Florida Current transports presented in the main text are based on the assimilation of submarine cable data over 1982–2018 with specified standard errors of 0.30–0.35 Sv (see Methods). To quantify how robust or sensitive the solutions are to the duration of the data and the selected standard errors, I perform two additional data assimilation experiments. In the first sensitivity experiment, I double the standard errors on the cable data given to the Bayesian algorithm during 1982–2018. I refer to this experiment as the "double-error" experiment. For clarity, in this section, I call the Bayesian model solution presented in the main text the "baseline" experiment. In the second sensitivity experiment, I maintain the original standard errors, but I give the Bayesian algorithm cable measurements for the period 2000–2018, withholding data values during 1982–1998. (Due to an outage in the observing system, no data are available for 1999.) I call this experiment the "half-data" experiment.

Salient features of the two sensitivity experiments are summarized alongside the baseline experiment in Supplementary Figure S13. Baseline and double-error solutions are, in many respects, very similar. For example, time series of Florida Current transport, transport trend over 1909–2018, and regression coefficient between transport and sea-level difference across the Florida Straits from these two experiments are nearly the same (cf. blue and orange in Supplementary Figure S13). One difference is that the widths of the posterior 95% credible intervals on the transport during 1982–

2018 (i.e., the period when transport observations are available) are about twice as large in the double-error experiment compared to the baseline experiment (Supplementary Figure S13a). This is consistent with the larger standard errors placed on the data in the former experiment. In sum, I conclude that model solutions are generally quantitatively insensitive to reasonable alternative specifications of the standard error on the cable transport measurements.

Solutions from the half-data experiment (yellow in Supplementary Figure S13) show similarities to the other two solutions, but can show larger uncertainty. This is unsurprising, since the half-data experiment has fewer data constraints. For example, whereas the posterior 95% credible intervals on the 110-y transport trend are -1.7 ± 3.7 and -1.6 ± 3.9 Sv century^{-1} in the baseline and double-error experiments, in the half-data experiment it is -2.3 ± 6.9 Sv century^{-1}. The fact that uncertainties from the double-error experiment are smaller than from the half-data experiment suggests that having more observations with larger errors is more informative for constraining the transport history than having fewer observations that have smaller errors. Importantly, although the trend from the half-data experiment is more uncertain in an absolute sense, the sign of the trend is similarly determined in all three experiments. I find that 82%, 80%, and 77% of trend solutions in the baseline, double-error, and half-data experiments are negative (Supplementary Figure S13b). That is, all three experiments suggest that Florida Current transport probably declined over the past century. Thus, I reason that the main findings in this study are qualitatively robust to reasonable alternative choices for the duration of the transport data assimilated into the Bayesian algorithm.

S4 Synthetic data experiments

In the half-data experiment, $\sim 90\%$ of the observed but withheld Florida Current transport values during 1982–1999 fall within the pointwise posterior 95% credible intervals on the transport. This suggests that the uncertainties estimated by the Bayesian algorithm are reasonable. To more thoroughly evaluate the meaningfulness of the posterior solutions generated by the Bayesian algorithm, I perform a number of synthetic data (or pseudo-proxy) experiments. In these experiments, I take a set of known processes and corrupt them to look like the observations, and I then apply the model to these corrupted process values. By comparing the posterior solutions to the known (withheld) values, I can quantify the accuracy and precision of the error bars furnished by the model (e.g., are $\sim 95\%$ of the true values actually captured by the posterior 95% credible intervals?).

First experiment—perfect model I run a perfect model experiment. I choose, from the ensemble of posterior model solutions presented in the main text, the array of scalar parameter solutions $\left(\overline{T}, r, \sigma^2, \ldots\right)$ from the ensemble member that minimizes the Mahalanobis distance to the mean parameter array. Using these scalar parameter values, I simulate synthetic versions of the sea-level and transport processes based on the process-level equations. Using the data-level equations, I generate synthetic tide-gauge and submarine-cable data by adding noise, bias, and gaps to the simulated processes, as in the real world, and I apply the Bayesian model to these synthetic data.

Results are summarized in Supplementary Table 7 and Supplementary Figure 14. For 13 out of the 14 scalar parameters, or $\sim 93\%$, the true value is captured by the corresponding 95% posterior credible interval from the model (Supplementary Table 7). Considering vector fields, I find that 100%, 98%, and 100% of the true values for regional sea-level trends $\boldsymbol{b}$, tide-gauge biases $\boldsymbol{\ell}$, and tide-gauge error trends $\boldsymbol{a}$ respectively fall within the corresponding pointwise posterior 95% credible intervals (not shown). In terms of the processes, 98% of the true sea-level values and 99% of true transport values fall within the estimated pointwise 95% credible intervals, and the true transport time series is entirely encompassed by the pathwise 95% posterior credible intervals (e.g., Supplementary Figure 14). Together, these results show that the model performs well, and that the posterior credible intervals are meaningful, if slightly conservative, roughly capturing the correct fraction of true process and parameter values.

Second experiment—more realistic case The first synthetic data experiment is informative, showing that the processes and parameters are identifiable given incomplete, noisy, biased data. It is also potentially idealistic, since the model is perfectly specified. The equations governing the spatiotemporal evolution of the processes, and the relationship between the observations and the processes were known perfectly, and the task was to infer the uncertain values of the processes and parameters appearing in those equations. While residual analysis suggests that they are appropriate given the data, the model equations probably represent a simplification of the complex, myriad oceanographic and geophysical processes contributing to changes in sea level and transport, and their correspondence to observations in the real world. While some degree of model misspecification is inevitable, the salient question is whether the model is robust to misspecification and still provides meaningful posterior estimates.

So, I perform a second synthetic data experiment. Rather than use the process equations to simulate sea level and transport, I bring together output from more complex physical models. I begin with ocean dynamics. I take 110 y of monthly Florida Current transport near 27°N, and sea level from each of the model grid cells nearest to the 46 tide gauges from version 2.2.4 of the Simple Ocean Data Assimilation (SODA) product[13]. This version of SODA represents a solution to an ocean general circulation model forced at the surface by an atmospheric reanalysis over the period 1871–2010 (I use the past 110 y of output covering from 1901 to 2010). The model has moderate spatial resolution, with 40 vertical levels and a native $0.25° \times 0.40°$ horizontal grid in longitude and latitude. A version of the solution, which was interpolated onto a regular $0.5° \times 0.5°$ horizontal grid, was downloaded from the Asia-Pacific Data-Research Center (APDRC) of the University of Hawai'i School of Ocean and Earth Science and Technology. After downloading I removed the monthly time series of global-mean sea level and computed annual means from the resulting monthly sea-level values.

The SODA solution represents a tradeoff between spatial resolution and temporal coverage. Coupled climate models are available that cover a comparable or longer time period[14], but most publicly available solutions have coarser horizontal resolution (nominally $\sim 1°$ in longitude and latitude), and may not faithfully represent the Florida Current and coastal sea level. While much higher-resolution ocean models are available[15] that more accurately portray the complexity of Florida Current transport and coastal sea level, these model runs are typically short, and do not span the centennial timescales of primary interest here. Thus, while it has its deficiencies (see below), SODA is perhaps one of the best-suited ocean models for my purposes. For example, Chepurin et al.[16] show that version 2.2.4 of SODA simulates interannual-to-decadal variations in coastal sea level along the eastern USA and parts of the Caribbean reasonably well over 1950–2011.

I superimpose static sea-level effects on the dynamic sea-level fields from SODA. I add a yearly time series of global-mean sea level due to ocean warming and thermal expansion over 1901–2010 from the Version 4 of the Community Climate System Model[17] (downloaded from the Woods Hole Oceanographic Institution's Community Storage Server). I also include, at each tide-gauge location, an estimate of the trend in relative sea level due to the combined effects of ongoing glacial isostatic adjustment from Peltier et al.[12] (downloaded from the PSMSL) along with twentieth-century melting of mountain glaciers and ice sheets due to Hamlington et al.[18] (courtesy of S. Adhikari, Jet Propulsion Laboratory). Finally, I add time series of a random-in-time but correlated-in-space process with zero mean and temporal variance of $\sim (1 \text{ cm})^2$ to simulate sea-level changes due to the inverted barometer effect linked with the North Atlantic Oscillation[19].

I apply the data-level equations to these transport and sea-level values, incorporating noise and bias, and imparting data gaps so that the synthetic tide-gauge and submarine-cable data are only available when and where the true observations are available. These synthetic datasets are subsequently fed into the Bayesian model algorithm. The results of this second synthetic data experiment are summarized in Supplementary Table 8 and Supplementary Figure 15. In this case, only four scalar parameters (those appearing in the data-level equations) are known perfectly. For three out of these four parameters, or 75%, the true value is captured by the 95% posterior credible intervals from the model (Supplementary Table 8). For one parameter, δ^2, the tide-gauge data error variance, the Bayesian model slightly underestimates the true value. Considering the process time series, I find that 81% of the true transport values and 95% of the true sea-level values are captured by the pointwise 95% posterior credible intervals produced by the Bayesian model, and that, as in the previous experiment, the full time series of the true transport is totally captured by the pathwise 95% posterior credible interval (Supplementary Figure 15).

It is worth noting that the posterior solution for α, the apparent trend in the transport process Eq. (4), suggests that sea level at Settlement Point on Grand Bahama must have risen 0.2 ± 1.6 mm y^{-1} faster than at West Palm Beach near West Palm Beach due to processes unrelated to ocean dynamics. This is consistent with the trend difference of ~ 0.1 mm y^{-1} I imposed between these two sites based on model estimates of GIA and contemporary ice melt[12,18], demonstrating that the model succeeds in separating static and dynamic sea-level trends.

Recall that my Bayesian model assumes that the transfer coefficient ρ between sea level and transport is a fixed constant. To test this assumption, I consider in more detail time series of Florida Current transport and sea-level difference across Florida Straits from SODA. Transport and sea-level difference are highly correlated with one another (Pearson correlation coefficient of ~ 0.9), and a linear regression suggests that transport increases by ~ 0.9 Sv for every 1-cm increase in sea level difference, consistent with a visual inspection of the two time series (Supplementary Figure 4a). To study the correspondence as a function of frequency band, I apply admittance and coherence analysis to the model output. Transport and sea-level difference are significantly coherent at all accessible periods from 2- to 32-y (Supplementary Figure 4b), in agreement with basic expectations from geostrophy. Moreover, the transfer function (using sea-level difference as the input and transport as the output) is qualitatively insensitive to frequency band, with similar values found at interannual and multidecadal timescales (Supplementary Figure 4c). Importantly, the Bayesian model posterior estimate for the transfer coefficient ρ is consistent with SODA and overlaps the values obtained from the admittance analysis (Supplementary Figure 4c). This suggests that it is reasonable to assume that there is a constant transfer coefficient between sea-level difference and transport on the timescales of this study, and also that the Bayesian model successfully infers the correct transfer-coefficient value.

Note that the Florida Current transport from SODA is suspicious (Supplementary Figure 15c). Mean transport is ~ 51 Sv, growing from ~ 42 Sv at the beginning of the period to ~ 56 Sv at the end. This value is $\sim 60\%$ larger than the average value observed by submarine cable since 1982, and ~ 10 Sv larger than the largest annual transport value inferred at any time in the original Bayesian model solution discussed in the main text. The striking increase of ~ 14 Sv over the 110-y run is extreme in light of the more subtle trend estimates produced by the original Bayesian model solution (cf. Figure 2a; Supplementary Figure 15c). Although it is imperfect, in that it does not realistically represent the true evolution of the Florida Current over the past century, SODA is nevertheless informative in the present context. For establishing the ability of the Bayesian algorithm to infer the parameters and processes from imperfect data, I do not require that the SODA reproduces observed reality, but rather that it portrays a physically plausible scenario, and that the basic "statistics" (e.g., spatiotemporal covariance structure, relationship between state variables, etc.) are believable.

In sum, I conclude that, even in a more complex setting, my Bayesian model performs reasonably well, giving uncertainty estimates that roughly capture the correct fraction of true values.

References

1. Rahmstorf, S., et al. Exceptional twentieth-century slowdown in Atlantic Ocean overturning circulation, *Nature Clim. Change*, **5**, 475–480 (2015).

2. Caesar, L., S. Rahmstorf, A. Robinson, G. Feulner, and V. Saba. Observed fingerprint of a weakening Atlantic Ocean overturning circulation, *Nature*, **556**, 191–196 (2018).

3. Thornalley, D. J. R., et al. Anomalously weak Labrador Sea convection and Atlantic overturning during the past 150 years, *Nature*, **556**, 227–230 (2018).

4. Drijfhout, S., et al. Is a Decline of AMOC Causing the Warming Hole above the North Atlantic in Observed and Modeled Warming Patterns?, *J. Clim.*, **25**, 8373–8379 (2012).

5. Roberts, C. D., F. K. Garry, and L. C. Jackson. A Multimodel Study of Sea Surface Temperature and Subsurface Density Fingerprints of the Atlantic Meridional Overturning Circulation, *J. Clim.*, **26**, 9155–9174 (2013).

6. Marshall, J., H. Johnson, and J. Goodman. A Study of the Interaction of the North Atlantic Oscillation with Ocean Circulation, *J. Clim.*, **14**, 1399–1421 (2001).

7. Large, W. G., and S. G. Yeager. Diurnal to Decadal Global Forcing For Ocean and Sea-Ice Models: The Data Sets and Flux Climatologies, *NCAR Technical Note*, NCAR/TN-460+STR, 112 pp.

8. Forget, G., et al. ECCO version 4: an integrated framework for non-linear inverse modeling and global ocean state estimation, *Geosci. Model Dev.*, **8**, 3071–3104 (2015).

9. Gebbie, G. Atlantic Warming Since the Little Ice Age, *Oceanography*, **32**, 220–230 (2019).

10. Thompson, P. R., and G. T. Mitchum. Coherent sea level variability on the North Atlantic western boundary, *J. Geophys. Res. Oceans*, **119**, 5676–5689, doi:10.1002/2014JC009999 (2014).

11. Zhao, J., and W. Johns. Wind-forced interannual variability of the Atlantic Meridional Overturning Circulation at $26.5°$N, *J. Geophys. Res.-Oceans*, **119**, 2403–2419.

12. Peltier, W. R., et al. Space geodesy constrains ice age terminal deglaciation: The global ICE-6G_C (VM5a) model, *J. Geophys. Res.-Solid Earth*, **120**, 450–487 (2015).

13. Giese, B. S., and S. Ray. El Niõ variability in simple ocean data assimilation (SODA), 1871–2008, *J. Geophys. Res.*, **116**, C02024 (2011).

14. Taylor, K. E., et al. An Overview of CMIP5 and the Experimental Design, *B. Am. Meteorol. Soc.*, **93**, 485–498 (2012).

15. Gula, J., M. J. Molemaker, and J. C. McWilliams. Topographic generation of submesoscale centrifugal instability and energy dissipation, *Nat. Commun.*, **7**, 12811 (2016).

16. Chepurin, G. A., J. A. Carton, and E. Leuliette. Sea level in ocean reanalyses and tide gauges, *J. Geophys. Res.-Oceans*, **119**, 147–155 (2014).

17. Gent, P. R., et al. The Community Climate System Model Version 4 , *J. Clim.*, **24**, 4973–4991 (2011).

18. Hamlington, B. D., et al. Observation-Driven Estimation of the Spatial Variability of 20th Century Sea Level Rise, *J. Geophys. Res.-Oceans*, **123**, 2129–2140 (2018).

19. Piecuch, C. G., and R. M. Ponte. Inverted barometer contributions to recent sea level changes along the northeast coast of North America, *Geophys. Res. Lett.*, **42**, 5918–5925 (2015).

20. Santamaría-Gómez, A., et al. Uncertainty of the 20th century sea-level rise due to vertical land motion errors, *Earth Planet. Sci. Lett.*, **473**, 24–32 (2017).

21. Love, R., et al. The contribution of glacial isostatic adjustment to projections of sea-level change along the Atlantic and Gulf coasts of North America, *Earth's Future*, **4**, 440–464 (2016).

22. Khan, N. S., et al. Drivers of Holocene sea-level change in the Caribbean, *Quaternary Sci. Rev.*, **155**, 13–36 (2017).

23. Gelman, A, and D. B. Rubin. Inference from iterative simulation using multiple sequences, *Stat. Sci.*, **7**, 457–472 (1992).

24. Birol, F., et al. Coastal applications from nadir altimetry: Example of the X-TRACK regional products, *Adv. Space Res.*, **59**, 936–953 (2017).

Region	Site	Lon (°W)	Lat (°N)	Duration (years)	Rate (mm y^{-1})	Error (mm y^{-1})
Florida	AOML	80.1622	25.7347	6.37	0.42	0.74
Florida	CCV6	80.5455	28.4600	6.93	-2.80	0.74
Florida	MIA3	80.1602	25.7328	11.00	-0.17	0.80
Bahamas	EXU0	75.8734	23.5640	6.50	-1.70	0.74
Bahamas	NAS0	77.4623	25.0525	6.51	-2.03	2.42

Table S1: **Summary of GPS data from Version 6a of the dataset from Université de la Rochelle[20] used to estimate the difference in static sea-level rate across Florida Straits due to differential land motion quoted in the main text.** Duration is the length of the data record. Error is twice the formal standard error provided with the dataset. Assuming errors are independent, the average rate across the two Bahamas sites is -1.87 ± 1.27 mm y^{-1} and the average rate across the three southeastern Florida sites is -0.85 ± 0.44 mm y^{-1}. The difference between the former and latter average values is -1.02 ± 1.34 mm y^{-1}, which represents the rate of differential vertical land motion across Florida Straits quoted in the main text. Multiplying by -1 to convert from the land-motion frame to the sea-level frame gives the value of 1.0 ± 1.3 mm y^{-1} quoted in the main text.

Region	Site	Reference	Lon (°W)	Lat (°N)	age (y BP)	sea level (m)
Florida	Florida Bay	Love et al.[21]	80.6	25	1260 ± 275	-1.34 ± 1.27
					890 ± 290	-0.83 ± 1.39
					400 ± 335	-1.00 ± 1.26
Florida	Bear Point	Love et al.[21]	80.3	27.4	1930 ± 350	-0.93 ± 1.45
					1380 ± 225	-1.13 ± 1.45
					1120 ± 215	-0.83 ± 1.45
Bahamas	Acklins Island	Khan et al.[22]	73.9	22.5	1048 ± 490	-1.64 ± 1.14
					698 ± 392	-1.23 ± 1.26
					398 ± 500	-1.08 ± 1.22
					242 ± 484	-0.97 ± 1.18

Table S2: **Proxy sea-level index points from southeastern Florida and the Bahamas used to estimate the difference in the rate of late-Holocene sea-level change across Florida Straits quoted in the main text.** Latitudes and longitudes have been rounded to the nearest tenth of a degree. The "y BP" abbreviation stands for years before present, where present is 1950. The $\pm$ values are twice the standard errors on the age and sea-level values provided in the given references. Using ordinary least squares to fit a trend line to the index points at each site, and ignoring age and sea-level uncertainty, I compute trends of 0.36 ± 0.97, 0.05 ± 0.73 and 0.81 ± 0.22 mm y^{-1} at Florida Bay, Bear Point, and Acklins Island, respectively, where $\pm$ is twice the formal standard error furnished by ordinary least squares assuming independent data. The average of the two trends from southeastern Florida is thus 0.20 ± 0.61 mm y^{-1} and so the difference between the Bahamas and southeastern Florida is 0.6 ± 0.6, which is the value quoted in the main text.

No.	Location	Lon (°E)	Lat (°N)	Timespan (Completeness)	Coast
1	Cristóbal	−79.9167	9.35	1909–1979 (100%)	904
2	Puerto Limon	−83.0333	10	1949–1968 (90%)	906
3	Cartagena	−75.55	10.4	1949–1992 (68%)	902
4	Riohacha	−72.9167	11.55	1953–1969 (82%)	902
5	Fort-de-France II	−61.0632	14.6015	2006–2017 (100%)	912
6	Santo Tomás de Castilla	−88.6167	15.7	1965–1980 (75%)	916
7	Puerto Cortes	−87.95	15.8333	1948–1968 (100%)	908
8	Puerto Castilla	−86.0333	16.0167	1956–1968 (100%)	908
9	Lime Tree Bay	−64.7533	17.6933	1986–2015 (80%)	939
10	Port Royal	−76.85	17.9333	1955–1969 (100%)	932
11	Magueyes Island	−67.045	17.97	1955–2016 (90%)	938
12	Barahona	−71.0833	18.2	1955–1969 (67%)	936
13	Charlotte Amalie	−64.92	18.335	1976–2016 (61%)	939
14	San Juan	−66.115	18.4583	1963–2016 (81%)	938
15	Port-au-Prince	−72.35	18.5667	1950–1961 (100%)	934
16	South Sound	−81.3833	19.2667	1976–1993 (89%)	931
17	North Sound	−81.3167	19.3	1976–1996 (86%)	931
18	Puerto Plata	−70.7	19.8167	1950–1969 (70%)	936
19	Cabo Cruz	−77.7333	19.8333	1993–2017 (76%)	930
20	Guantanamo Bay	−75.1467	19.9067	1938–1971 (85%)	930
21	Gibara	−76.125	21.1083	1976–2016 (100%)	930
22	Nuevitas Punta Practico	−77.1095	21.5913	1992–2017 (35%)	930
23	Casilda II	−79.9917	21.7533	1984–2014 (48%)	930
24	Cabo de San Antonio	−84.9	21.9	1973–2017 (60%)	930
25	Isabela de Sagua	−80.0167	22.9333	2000–2016 (71%)	930
26	Key West	−81.8067	24.555	1913–2018 (97%)	940
27	Vaca Key	−81.105	24.7117	1990–2017 (79%)	940
28	Key Colony Beach	−81.0167	24.7183	1978–1994 (71%)	940
29	Virginia Key	−80.1617	25.73	1995–2017 (87%)	960
30	Miami Beach	−80.1317	25.7683	1932–1980 (92%)	960
31	Naples	−81.8067	26.1317	1966–2017 (83%)	940
32	West Palm Beach	−80.0333	26.6117	1974–2017 (36%)	960
33	Settlement Point	−78.9833	26.6833	2005–2015 (82%)	941
34	Settlement Point	−78.9967	26.71	1986–2000 (67%)	941
35	Trident Pier	−80.5917	28.415	1995–2017 (91%)	960
36	Daytona Beach Shores	−80.9633	29.1467	1967–1983 (71%)	960
37	Daytona Beach	−81	29.2333	1925–1969 (51%)	960
38	Jacksonville	−81.6167	30.35	1954–1967 (100%)	960
39	Mayport	−81.4317	30.3933	1929–1999 (99%)	960
40	Mayport	−81.4283	30.3983	2001–2017 (94%)	960
41	Fernandina Beach	−81.465	30.6717	1909–2018 (78%)	960
42	Fort Pulaski	−80.9017	32.0333	1935–2018 (95%)	960
43	Charleston	−79.925	32.7817	1922–2018 (100%)	960
44	Springmaid Pier	−78.9183	33.655	1978–2017 (60%)	960
45	Myrtle Beach	−78.885	33.6833	1958–1977 (55%)	960
46	Wilmington	−77.9533	34.2267	1936–2018 (95%)	960

Table S3: **Descriptions of tide-gauge sea-level records used in this study.** "Completeness" is the percentage of timespan during which data are available. "Coast" number is the code used by the PSMSL to indicate the country and coastline of measurement.

Parameter	Description
$\boldsymbol{\eta}_0$	Sea-level initial condition
$\boldsymbol{\eta}_k$	Sea-level values at time t_k
$\overline{T}$	Transport time-mean value
T_k	Transport value at time t_k
$\boldsymbol{b}$	Spatial vector of regional trends in sea level
$\boldsymbol{a}$	Spatial vector of local trends in sea level
$\boldsymbol{\ell}$	Spatial vector of tide-gauge biases
r	AR(1) coefficient of sea level
μ	Mean value of regional trends in sea level
ν	Mean value of tide-gauge biases
ρ	Transport change per unit sea-level difference
α	Transport trend correction
π^2	Partial sill of regional trends in sea level
σ^2	Partial sill of sea-level innovations
δ^2	Tide-gauge error variance
τ^2	Spatial variance in observational biases
γ^2	Variance of local trends in sea level
ω^2	Variance of transport noise correction
ϕ	Inverse range of sea-level innovations
λ	Inverse range of regional trends in sea level

Table S4: **Descriptions of model processes and parameters.**

Parameter	Prior Distribution	Hyperparameter Values
$\boldsymbol{\eta}_0$	$\mathcal{N}\left(\tilde{\eta}_{\boldsymbol{\eta}_0}\mathbf{1}, \tilde{\zeta}^2_{\boldsymbol{\eta}_0}\mathsf{I}\right)$	$\tilde{\eta}_{\boldsymbol{\eta}_0} = -0.2 \text{ m}\ ,\ \tilde{\zeta}^2_{\boldsymbol{\eta}_0} = (7.6 \times 10^{-2} \text{ m})^2$
$\overline{T}$	$\mathcal{N}\left(\tilde{\eta}_{\overline{T}}, \tilde{\zeta}^2_{\overline{T}}\right)$	$\tilde{\eta}_{\overline{T}} = 32 \text{ Sv}\ ,\ \tilde{\zeta}^2_{\overline{T}} = (5.2 \text{ Sv})^2$
r	$\mathcal{U}\left(\tilde{u}_r, \tilde{v}^2_r\right)$	$\tilde{u}_r = 0.0\ ,\ \tilde{v}^2_r = 1.0$
μ	$\mathcal{N}\left(\tilde{\eta}_\mu, \tilde{\zeta}^2_\mu\right)$	$\tilde{\eta}_\mu = 3.4 \times 10^{-3} \text{ m y}^{-1}\ ,\ \tilde{\zeta}^2_\mu = (2.7 \times 10^{-2} \text{ m y}^{-1})^2$
ν	$\mathcal{N}\left(\tilde{\eta}_\nu, \tilde{\zeta}^2_\nu\right)$	$\tilde{\eta}_\nu = 7.0 \text{ m}\ ,\ \tilde{\zeta}^2_\nu = (0.6 \text{ m})^2$
ρ	$\mathcal{N}\left(\tilde{\eta}_\rho, \tilde{\zeta}^2_\rho\right)$	$\tilde{\eta}_\rho = 0.0 \text{ Sv m}^{-1}\ ,\ \tilde{\zeta}^2_\rho = (190 \text{ Sv m}^{-1})^2$
α	$\mathcal{N}\left(\tilde{\eta}_\alpha, \tilde{\zeta}^2_\alpha\right)$	$\tilde{\eta}_\alpha = 0.0 \text{ Sv y}^{-1}\ ,\ \tilde{\zeta}^2_\alpha = (0.3 \text{ Sv y}^{-1})^2$
π^2	$\mathcal{IG}\left(\tilde{\xi}_{\pi^2}, \tilde{\chi}^2_{\pi^2}\right)$	$\tilde{\xi}_{\pi^2} = 0.5\ ,\ \tilde{\chi}^2_{\pi^2} = (1.9 \times 10^{-3} \text{ m y}^{-1})^2$
σ^2	$\mathcal{IG}\left(\tilde{\xi}_{\sigma^2}, \tilde{\chi}^2_{\sigma^2}\right)$	$\tilde{\xi}_{\sigma^2} = 0.5\ ,\ \tilde{\chi}^2_{\sigma^2} = (1.8 \times 10^{-2} \text{ m})^2$
δ^2	$\mathcal{IG}\left(\tilde{\xi}_{\delta^2}, \tilde{\chi}^2_{\delta^2}\right)$	$\tilde{\xi}_{\delta^2} = 0.5\ ,\ \tilde{\chi}^2_{\delta^2} = (7.1 \times 10^{-3} \text{ m})^2$
τ^2	$\mathcal{IG}\left(\tilde{\xi}_{\tau^2}, \tilde{\chi}^2_{\tau^2}\right)$	$\tilde{\xi}_{\tau^2} = 0.5\ ,\ \tilde{\chi}^2_{\tau^2} = (8.5 \times 10^{-2} \text{ m})^2$
γ^2	$\mathcal{IG}\left(\tilde{\xi}_{\gamma^2}, \tilde{\chi}^2_{\gamma^2}\right)$	$\tilde{\xi}_{\gamma^2} = 0.5\ ,\ \tilde{\chi}^2_{\gamma^2} = (7.1 \times 10^{-4} \text{ m y}^{-1})^2$
ω^2	$\mathcal{IG}\left(\tilde{\xi}_{\omega^2}, \tilde{\chi}^2_{\omega^2}\right)$	$\tilde{\xi}_{\omega^2} = 0.5\ ,\ \tilde{\chi}^2_{\omega^2} = (0.7 \text{ Sv})^2$
ϕ	$\mathcal{LN}\left(\tilde{\eta}_\phi, \tilde{\zeta}^2_\phi\right)$	$\tilde{\eta}_\phi = -7.0 \log \text{km}^{-1}\ ,\ \tilde{\zeta}^2_\phi = (2.2 \log \text{km}^{-1})^2$
λ	$\mathcal{LN}\left(\tilde{\eta}_\lambda, \tilde{\zeta}^2_\lambda\right)$	$\tilde{\eta}_\lambda = -6.9 \log \text{km}^{-1}\ ,\ \tilde{\zeta}^2_\lambda = (0.4 \log \text{km}^{-1})^2$

Table S5: **Prior distributions and hyperparameters.** Hyperparameters are denoted with tildes to distinguish them from the other (uncertain) model parameters. The scripts are: $\mathcal{N}$ normal (or multivariate normal) distribution with mean $\tilde{\eta}$ and variance $\tilde{\zeta}^2$; $\mathcal{U}$ uniform distribution with lower bound $\tilde{u}$ and upper bound $\tilde{v}$; $\mathcal{IG}$ inverse-gamma distribution with shape ξ and scale χ; $\mathcal{LN}$ log-normal distribution with "mean" $\tilde{\eta}$ and "variance" $\tilde{\zeta}^2$.

Parameter	Units	$\hat{R}$	Median Value	95% CI	Width Ratio
$\overline{T}$	Sv	1.001	32.6317	$[31.2047,\ 34.0538]$	0.13837
α	Sv y^{-1}	1.0007	-0.013584	$[-0.054013,\ 0.0293]$	0.085205
r	—	1.0066	0.55246	$[0.47413,\ 0.63057]$	0.16441
$\mu\ (\times 10^3)$	m y^{-1}	1.0007	2.6671	$[1.1105,\ 4.2612]$	0.028929
ν	m	0.99976	6.9845	$[6.9619,\ 7.0065]$	0.018982
ρ	Sv m^{-1}	0.9996	21.3501	$[10.4544,\ 32.4271]$	0.029465
$\pi^2\ (\times 10^6)$	$(\text{m y}^{-1})^2$	1.0001	$(1.1673)^2$	$[(0.75971)^2,\ (1.9104)^2]$	0.00056614
$\sigma^2\ (\times 10^6)$	m^2	1.0019	$(26.2588)^2$	$[(24.4292)^2,\ (28.3339)^2]$	0.00024641
$\delta^2\ (\times 10^6)$	m^2	0.99995	$(8.3539)^2$	$[(7.3177)^2,\ (9.4754)^2]$	0.00037666
$\tau^2\ (\times 10^6)$	m^2	0.99973	$(66.9832)^2$	$[(54.0808)^2,\ (85.3079)^2]$	0.00040194
$\gamma^2\ (\times 10^6)$	$(\text{m y}^{-1})^2$	0.99995	$(0.6992)^2$	$[(0.40244)^2,\ (1.1171)^2]$	0.00090338
ω^2	Sv^2	0.9997	$(0.708)^2$	$[(0.4832)^2,\ (1.0033)^2]$	0.00058865
$\phi\ (\times 10^3)$	km^{-1}	1.0025	0.68742	$[0.52277,\ 0.87158]$	0.0040641
$\lambda\ (\times 10^3)$	km^{-1}	1.0005	0.8429	$[0.43847,\ 1.6407]$	0.80349

Table S6: **Summary of posterior solutions for scalar parameters.** The symbol $\hat{R}$ is a convergence monitor of Gelman and Rubin[23], such that values near 1 indicate convergence. Median Value and 95% credible interval (CI) are computed from the ensemble of posterior model solutions. The Width Ratio is defined as ratio of the width of the posterior 95% CI to the prior 95% CI width.

Parameter	Units	Truth	Median Value	95% CI
$\overline{T}$	Sv	32.8942	32.0523	$[30.9524,\ 33.0873]$
α	Sv y^{-1}	-0.018899	-0.023436	$[-0.059135,\ 0.0090315]$
r	—	0.54595	0.53247	$[0.46355,\ 0.60654]$
$\mu\ (\times 10^3)$	m y^{-1}	2.977	3.1574	$[1.2438,\ 5.1438]$
ν	m	6.9876	6.9947	$[6.9739,\ 7.0165]$
ρ	Sv m^{-1}	23.5497	20.974	$[14.9067,\ 27.6991]$
$\pi^2\ (\times 10^6)$	$(\text{m y}^{-1})^2$	$(1.078)^2$	$(1.4473)^2$	$[(0.94505)^2,\ (2.2444)^2]$
$\sigma^2\ (\times 10^6)$	m^2	$(26.443)^2$	$(25.5557)^2$	$[(23.6732)^2,\ (27.7207)^2]$
$\delta^2\ (\times 10^6)$	m^2	$(8.7092)^2$	$(9.2437)^2$	$[(8.3297)^2,\ (10.1856)^2]$
$\tau^2\ (\times 10^6)$	m^2	$(67.1828)^2$	$(66.178)^2$	$[(54.0051)^2,\ (83.3185)^2]$
$\gamma^2\ (\times 10^6)$	$(\text{m y}^{-1})^2$	$(0.64645)^2$	$(0.80521)^2$	$[(0.54918)^2,\ (1.1481)^2]$
ω^2	Sv^2	$(0.77083)^2$	$(0.34671)^2$	$[(0.23695)^2,\ (0.51894)^2]$
$\phi\ (\times 10^3)$	km^{-1}	0.63572	0.60636	$[0.46714,\ 0.78344]$
$\lambda\ (\times 10^3)$	km^{-1}	0.79168	0.83584	$[0.44534,\ 1.6007]$

Table S7: **Summary of first synthetic data experiment.** Comparison between the true (withheld) parameter values and the posterior model estimates.

Parameter	Units	True Value	Median Value	95% CI
ν	m	6.9876	6.9707	$[6.9506,\ 6.9918]$
δ^2 $(\times 10^6)$	m^2	$(8.7092)^2$	$(7.2674)^2$	$[(6.4296)^2,\ (8.1361)^2]$
τ^2 $(\times 10^6)$	m^2	$(67.1828)^2$	$(62.0712)^2$	$[(50.8668)^2,\ (78.9978)^2]$
γ^2 $(\times 10^6)$	$(\mathrm{m\ y}^{-1})^2$	$(0.64645)^2$	$(0.80316)^2$	$[(0.55894)^2,\ (1.1291)^2]$

Table S8: **Summary of second synthetic data experiment.** Comparison between the true (withheld) parameter values and the posterior model estimates.

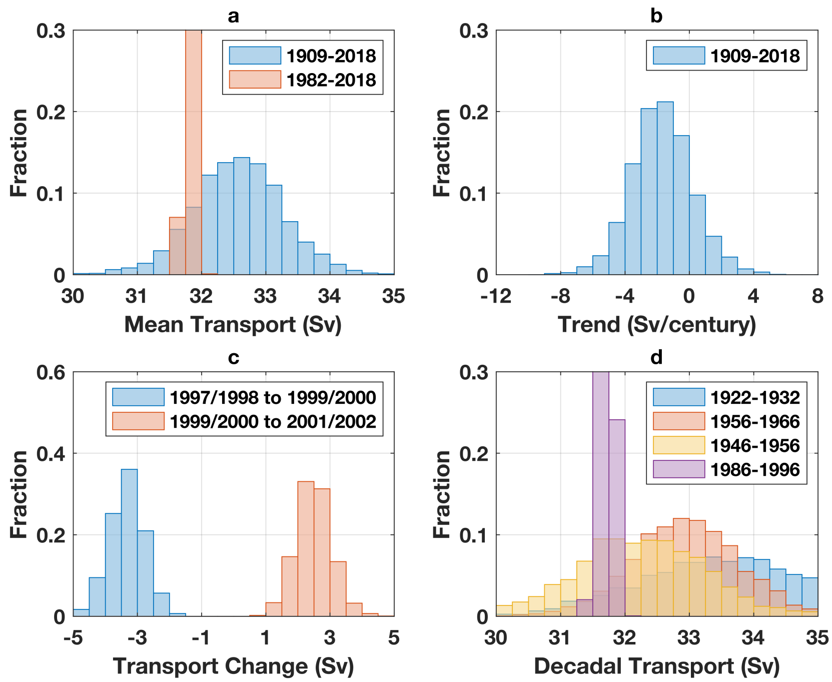

Figure S1 **Some aspects of the posterior solution.** **a,** Blue (orange) is the histogram of the mean of the transport $\boldsymbol{T}$ in units of Sv over the 1909–2018 study period (1982–2018). **b,** Histogram of the transport trend $\rho \boldsymbol{b}^{\mathsf{T}} \boldsymbol{\Delta} + \alpha$ over 1909–2018 (Sv century^{-1}). **c,** Blue (orange) is the histogram of the change in transport $\boldsymbol{T}$ in units of Sv between 1997/1998 to 1999/2000 (1999/2000 to 2001/2002). **d,** Histograms of decadally averaged transport $\boldsymbol{T}$ in units of Sv: blue 1922–1932; orange 1956–1966; yellow 1946–1956; and purple 1986–1996. See Supplementary Table 4 for descriptions of symbols.

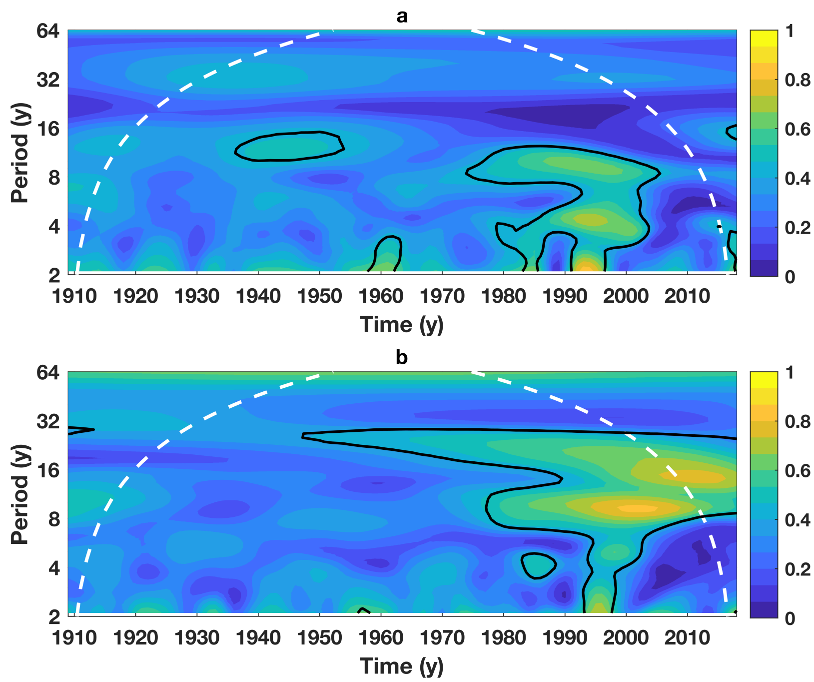

Figure S2 **Wavelet coherences.** Magnitude squared wavelet coherence between Florida Current transport T and **a,** North Atlantic Oscillation and **b,** Atlantic Multidecadal Variability. Values are computed as follows. For each ensemble member, the wavelet coherence is computed between the transport solution and the climate index. For the same ensemble member, two random time series are generated, which have identical Fourier amplitudes to the transport solution and climate index, but randomized phases, and the wavelet coherence between the random time series is computed. Shaded colors represent medians of the set of wavelet-coherence values computed between all transport solutions and the given climate index. Black contouring indicates where 68% of wavelet coherences computed between transport solutions and the climate index exceed the value calculated between the pairs of random time series.

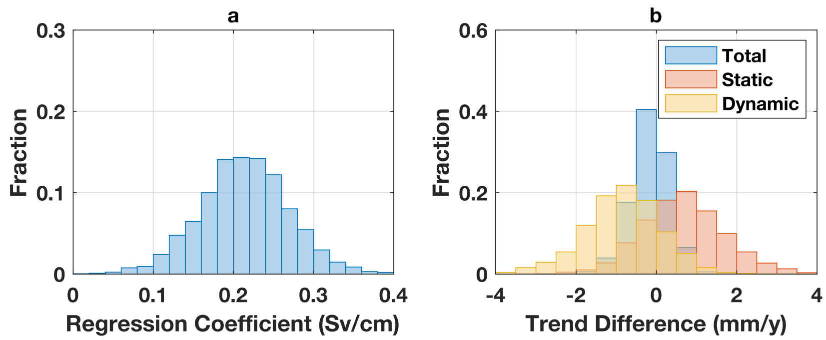

Figure S3 **More aspects of the posterior solution.** **a,** Histogram of posterior solutions for the regression coefficient ρ (Sv cm^{-1}) between sea-level difference across Florida Straits and Florida Current transport. **b,** Histogram of posterior solutions for the total (blue), static (orange), and dynamic (yellow) trends in sea-level difference across Florida Straits, which are computed respectively as $\boldsymbol{b}^{\mathsf{T}}\boldsymbol{\Delta}$, $-\alpha/\rho$, and $\boldsymbol{b}^{\mathsf{T}}\boldsymbol{\Delta} + \alpha/\rho$ (mm y^{-1}) (cf. Methods). See Supplementary Table 4 for descriptions of symbols.

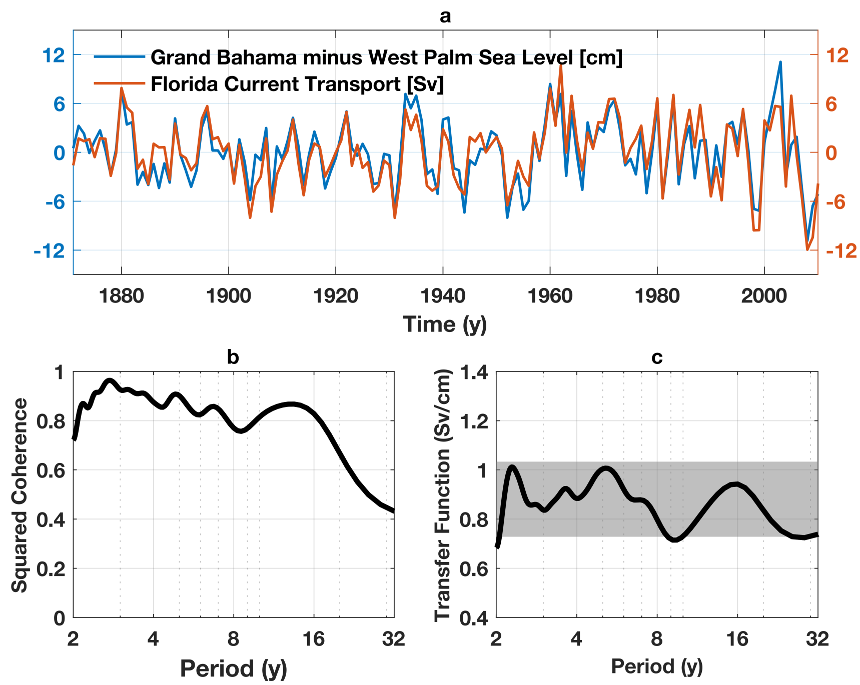

Figure S4 **Sea level and transport from SODA. a,** Blue (orange) is the annual time series of sea-level difference across Florida Straits between Grand Bahama and West Palm Beach (Florida Current transport) during 1871–2010 from the SODA ocean model solution. Note that both time series have been detrended. **b,** Black line is magnitude-squared coherence between sea-level difference and transport the first 128 y of the SODA model solution (1871–1998). All values are statistically significant at the 95% confidence level based on comparison against calculations with synthetic time series. **c,** Black line is amplitude of the transfer function from an admittance calculation using sea-level difference as the input and transport as the output. Gray shading is the 95% posterior credible interval on the transfer coefficient ρ from a synthetic data experiment based on the SODA model solution (see Supplementary Information). Admittance and coherence calculations are based on Welch's method using a window length of 32 and 50% overlap.

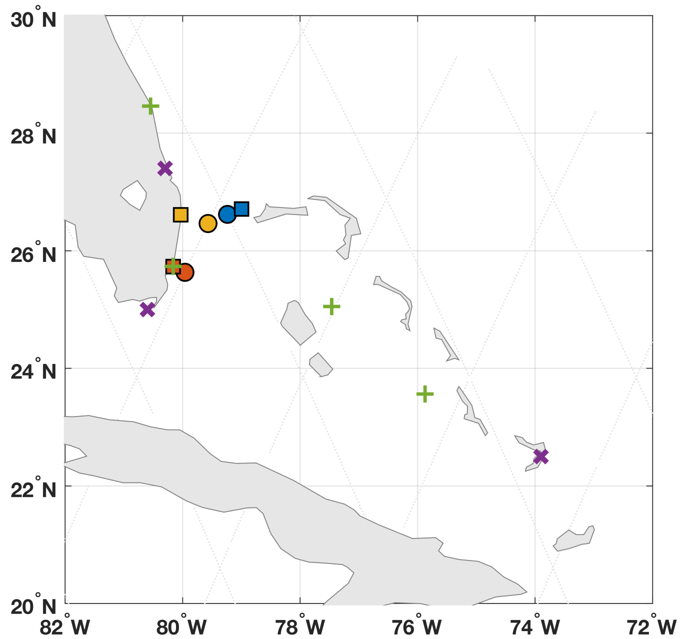

Figure S5 **Locations of ancillary observational assets.** Shaded squares are tide-gauge locations (blue is Settlement Point; orange is Virginia Key; yellow is West Palm Beach). Shaded circles are the along-track satellite-altimeter data points that are nearest the corresponding tide gauge. Light gray criss-crossing marks ascending and descending altimeter tracks. Green + symbols denote locations of GPS stations (cf. Supplementary Table 1). Purple $\times$ symbols are the locations of proxy sea-level indicators (cf. Supplementary Table 2).

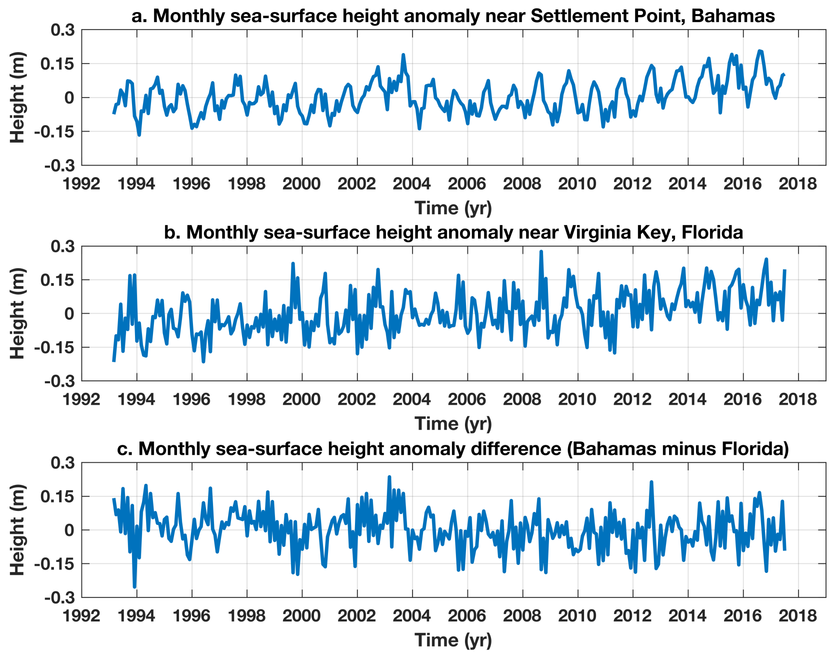

Figure S6 **Altimetric sea-surface height.** Monthly time series of anomalous sea-surface height from satellite altimetry near **a,** Settlement Point, Bahamas, **b,** Virginia Key, Florida, and **c,** the difference between the two time series. Values shown here are calculated by bin averaging the raw 1-Hz data provided by Birol et al.[24] by year and month. A mean seasonal cycle (annual and semi-annual harmonics) has been removed in each case. See Supplementary Figure S5 for the locations of the time series.

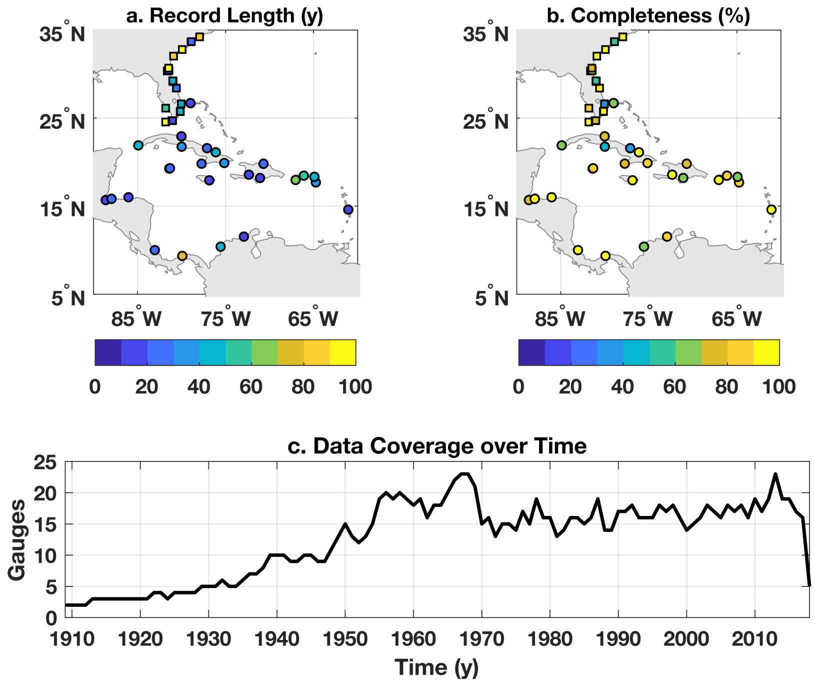

Figure S7 **Characteristics of tide-gauge data.** **a,** Record length of tide-gauge records (number of y between the first and last measurements made during the study period). Yellower (bluer) colors indicate longer (shorter) records. **b,** Record completeness (percentage of y during the record length for which annual data are available). Yellower (bluer) colors indicate more (less) complete records. **c,** Number of tide gauges returning annual sea-level data during the course of the study period.

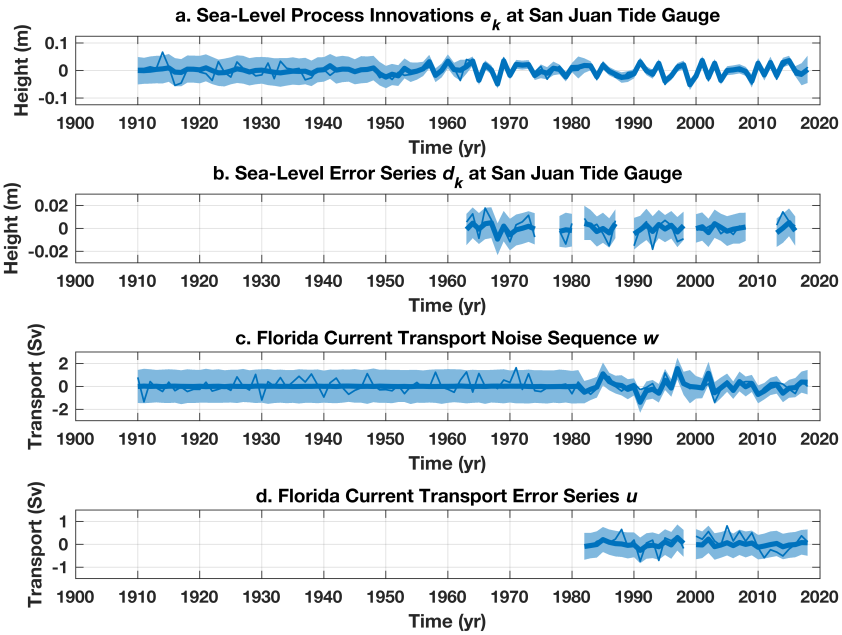

Figure S8 **Examples of residual time series.** Posterior median (solid lines) and pointwise 95% credible intervals (light shading) of the sea-level **a,** process innovations e_k and **b,** data errors d_k at the San Juan (Puerto Rico) tide gauge. Posterior median (solid lines) and pointwise 95% credible intervals (light shading) of the transport **c,** noise sequence w_k and **d,** data errors u_k.

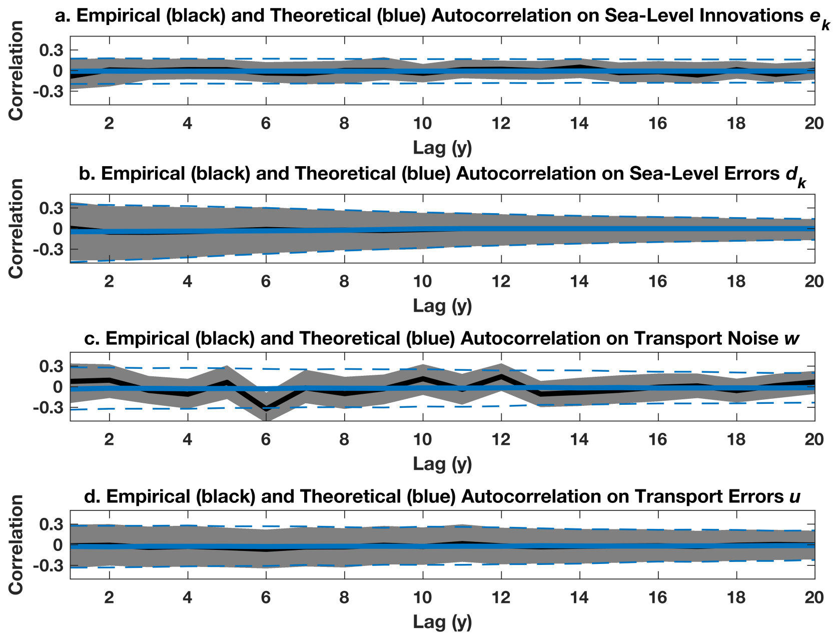

Figure S9 **Autocorrelation of the residuals.** Posterior medians (solid black) and pointwise 95% credible intervals (gray shading) of the sample autocorrelation coefficient computed empirically from posterior solutions for the **a,** sea-level process innovations e_k, **b,** sea-level data errors d_k, **c,** transport noise sequence w_k, and **d,** transport data errors u_k. Solid and dashed blue lines are the mean $\pm$ twice the standard error on the autocorrelation coefficients expected theoretically from white noise with the same temporal degrees of freedom.

411

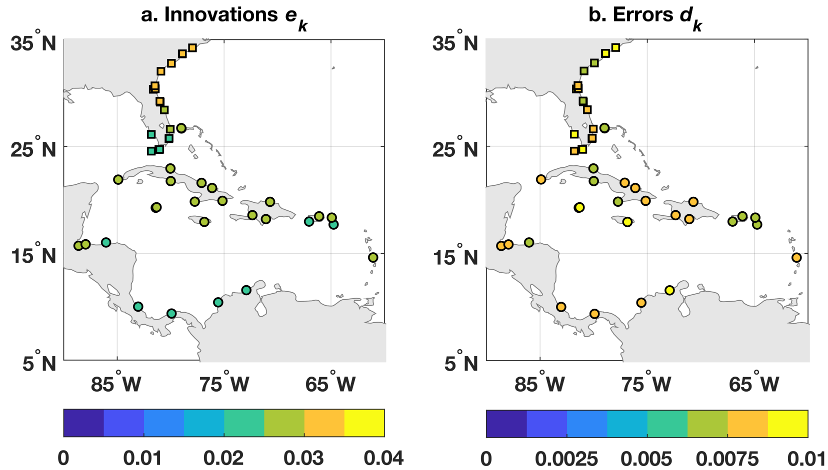

412 **Figure S10** **Amplitude of sea-level residual time series.** Median values of the standard
413 deviation (m) computed from posterior solutions for the sea-level **a,** process innovations
414 e_k and **b,** data errors d_k at all tide-gauge locations.

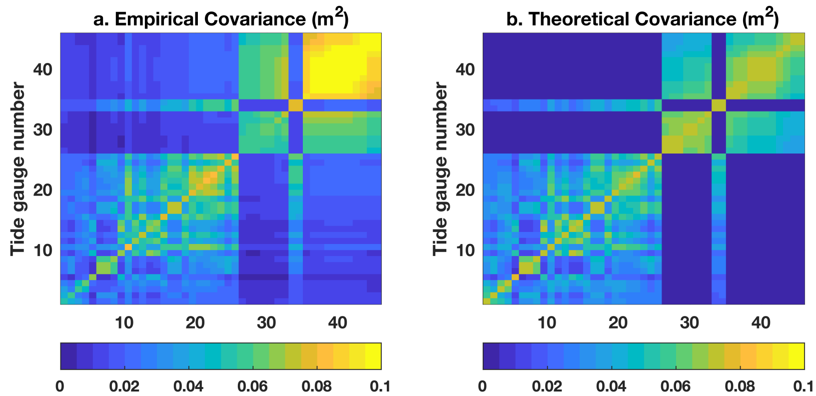

Figure S11 **Spatial covariance of sea-level process innovations.** Covariance (m^2) between all pairs of sea-level process innovations $\boldsymbol{e}_k$ computed **a,** empirically based on posterior solutions for $\boldsymbol{e}_k$ and **a,** theoretically using posterior solutions for σ^2 (Supplementary Table 6) and the assumed covariance structure Eq. (2). The "tide-gauge number" along x- and y-axes refer to the values given in the leftmost column in Supplementary Table 3.

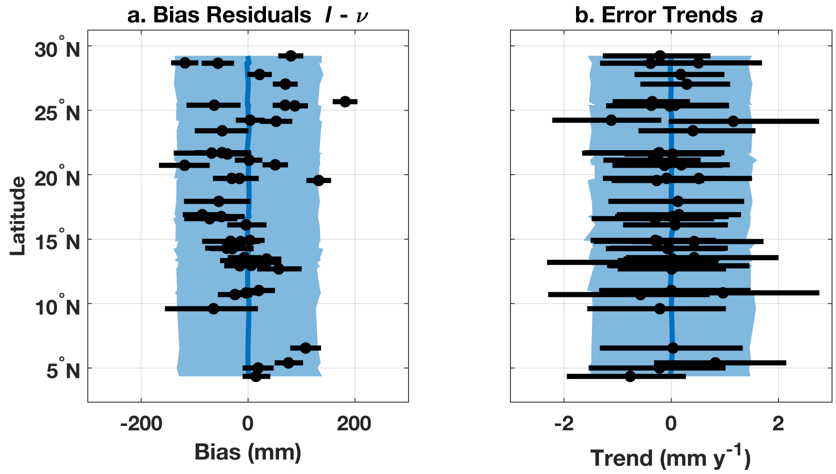

Figure S12 **Spatial structure of tide-gauge residual vectors.** Posterior medians (black dots) and pointwise 95% credible intervals (black lines) for the tide-gauge **a,** data-bias anomalies $\boldsymbol{\ell} - \nu\mathbf{1}$ (m) and **b,** error trends $\boldsymbol{a}$ (mm y^{-1}). Also shown are the means (solid blue) and 95% credible intervals on these fields estimated from their assumed functional forms and posterior solutions for the respective variance parameters τ^2 and γ^2 (Supplementary Table 6).

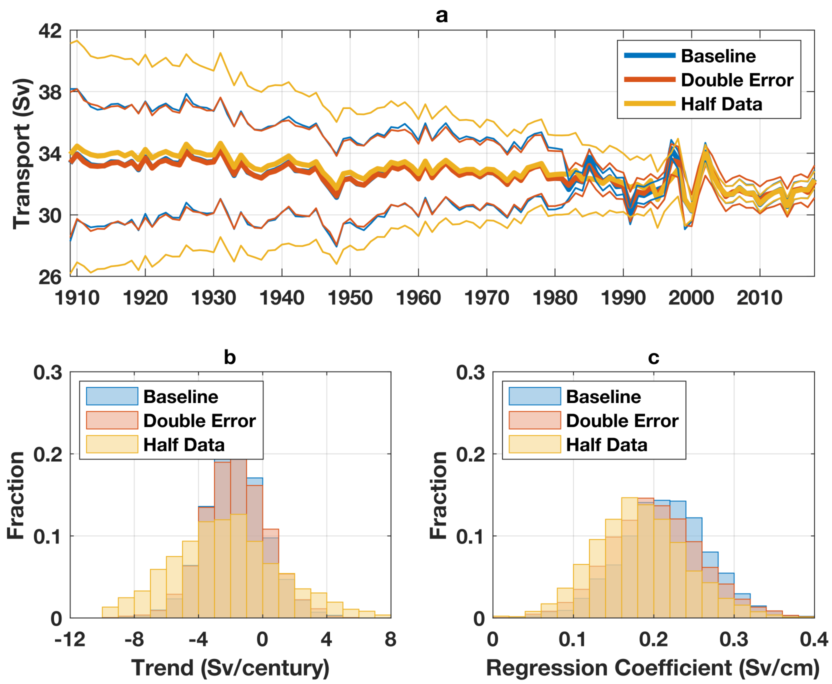

Figure S13 **Sensitivity of Bayesian model solution to input transport data.** Summary of results from sensitivity experiments using different forms of the Florida Cable transport data. **a,** Time series of transport (thick lines are posterior medians; thin lines bound the posterior 95% pointwise credible intervals). **b,** Histograms of the 110-y trend (1909–2018) in Florida Current transport. **c,** Regression coefficient between sea-level difference across Florida Straits and Florida Current transport. Blue values are from the "baseline" model experiment discussed in the main text. Orange values are based on an "double error" experiment wherein the standard errors on the transport data during 1982–2018 are doubled. Yellow values are based on a "half data" experiment where the algorithm is only given the cable data during the period 2000–2018 and the 1982–1998 values are withheld. (There is no transport data value for 1999 due to a 20-month outage in the cable observations.)

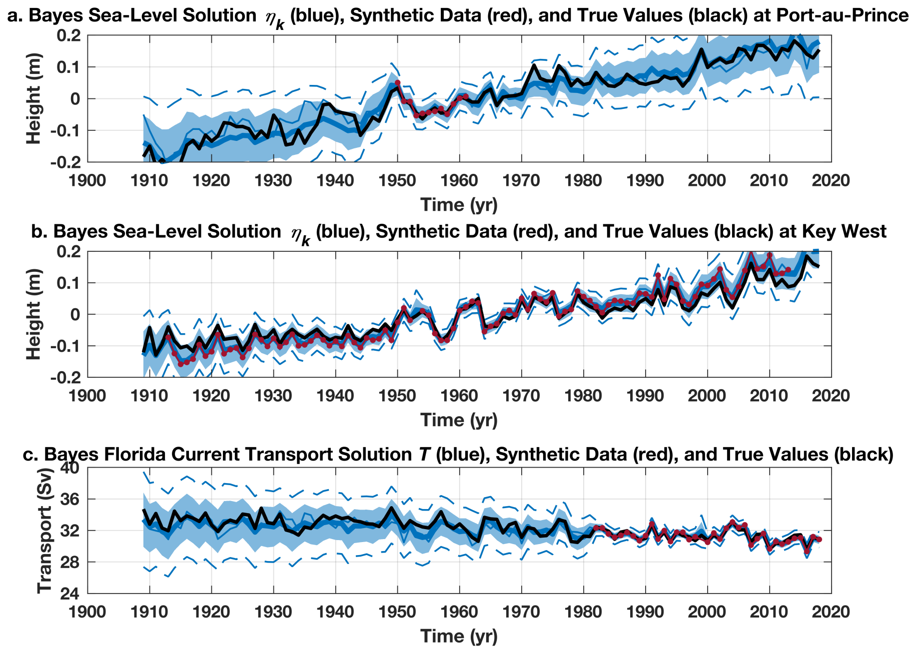

Figure S14 **Examples of results from first synthetic data experiment.** Synthetic observations (red), true values (black), and posterior medians (thick blue), pointwise (blue shading) and pathwise (dashed blue) 95% credible intervals, and an arbitrary ensemble member (thin blue) of **a,** sea level at the Port-au-Prince (Haiti) tide gauge, **a,** sea level at the Key West (USA) tide gauge, and **c,** Florida Current transport.

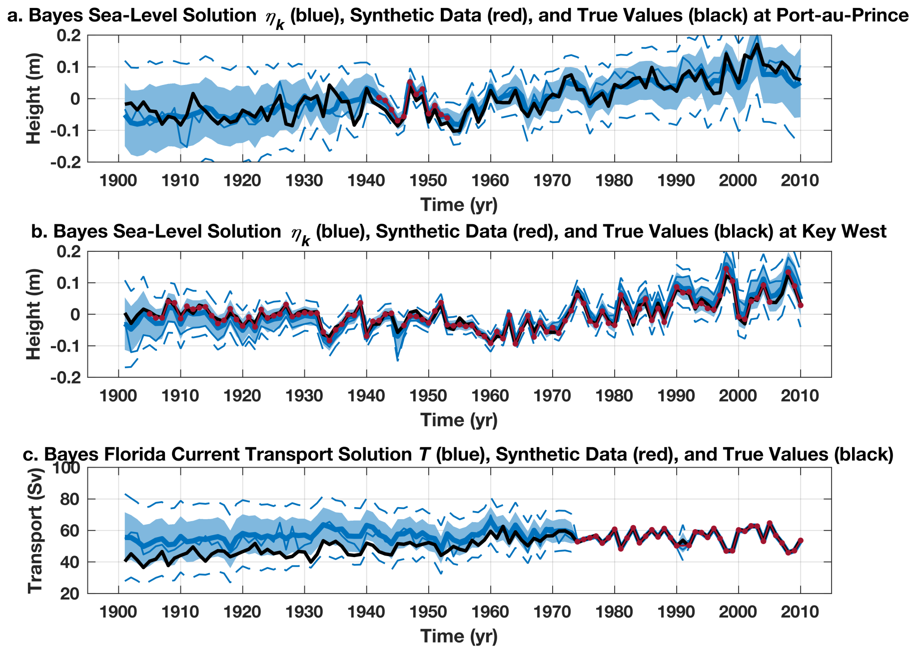

Figure S15 **Examples of results from second synthetic data experiment.** Synthetic observations (red), true values (black), and posterior medians (thick blue), pointwise (blue shading) and pathwise (dashed blue) 95% credible intervals, and an arbitrary ensemble member (thin blue) of **a,** sea level at the Port-au-Prince (Haiti) tide gauge, **a,** sea level at the Key West (USA) tide gauge, and **c,** Florida Current transport.